

---

# **STRUCTURAL COMPOSITE PENETRATION MODEL DEVELOPMENT**

**Jinn-Kuen Chen et al.**

**October 1996**

**Final Report**

19970114 071

---

**APPROVED FOR PUBLIC RELEASE; DISTRIBUTION IS UNLIMITED.**

---



**PHILLIPS LABORATORY**  
**Advanced Weapons and Survivability Directorate**  
**AIR FORCE MATERIEL COMMAND**  
**KIRTLAND AIR FORCE BASE, NM 87117-5776**

Using Government drawings, specifications, or other data included in this document for any purpose other than Government procurement does not in any way obligate the U.S. Government. The fact that the Government formulated or supplied the drawings, specifications, or other data, does not license the holder or any other person or corporation; or convey any rights or permission to manufacture, use, or sell any patented invention that may relate to them.

This report has been reviewed by the Public Affairs Office and is releasable to the National Technical Information Service (NTIS). At NTIS, it will be available to the general public, including foreign nationals.

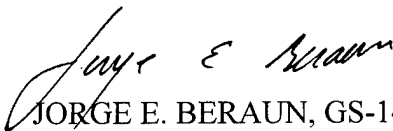
If you change your address, wish to be removed from this mailing list, or your organization no longer employs the addressee, please notify PL/WSAE, 3550 Aberdeen Ave SE, Kirtland AFB, NM 87117-5776.

Do not return copies of this report unless contractual obligations or notice on a specific document requires its return.

This report has been approved for publication.



JINN-KUEN CHEN  
Project Manager, GS-13



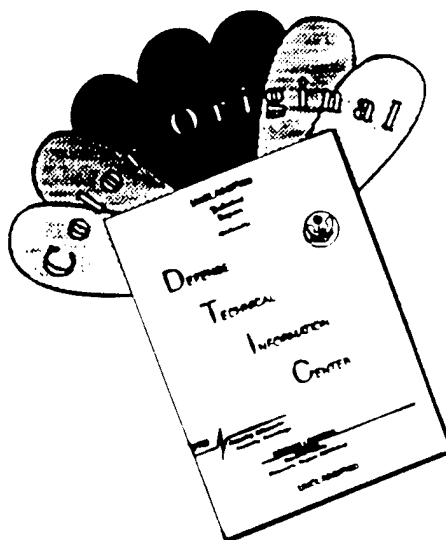
JORGE E. BERAUN, GS-14  
Chief, Laser Effects Branch

FOR THE COMMANDER



WILLIAM G. HECKATHORN, Col, USAF  
Director, Advanced Weapons and  
Survivability Directorate

# DISCLAIMER NOTICE



THIS DOCUMENT IS BEST QUALITY AVAILABLE. THE COPY FURNISHED TO DTIC CONTAINED A SIGNIFICANT NUMBER OF COLOR PAGES WHICH DO NOT REPRODUCE LEGIBLY ON BLACK AND WHITE MICROFICHE.

# DRAFT SF 298

<b>1. Report Date (dd-mm-yy)</b> October 1996		<b>2. Report Type</b> Final Report		<b>3. Dates covered (from... to )</b> 20 Mar 95 - 06 Feb 96	
<b>4. Title &amp; subtitle</b>  STRUCTURAL COMPOSITE PENETRATION MODEL DEVELOPMENT			<b>5a. Contract or Grant #</b> WAL-5-3063		
			<b>5b. Program Element #</b> 62201F		
<b>6. Author(s)</b>  Jinn-Kuen Chen Firooz A. Allahdadi			<b>5c. Project #</b> 2402		
			<b>5d. Task #</b> 02		
			<b>5e. Work Unit #</b> 61		
<b>7. Performing Organization Name &amp; Address</b> Phillips Laboratory PL/WSAE 3550 Aberdeen Ave SE Kirtland AFB, NM 87117-5776				<b>8. Performing Organization Report #</b>  PL-TR-96-1140	
<b>9. Sponsoring/Monitoring Agency Name &amp; Address</b> Wright Laboratory WL/FIVSM 1901 Tenth Street, Bldg. 63 Wright Patterson AFB, OH 45433-7605				<b>10. Monitor Acronym</b> WL/FIVSM	
				<b>11. Monitor Report #</b>	
<b>12. Distribution/Availability Statement</b>  Approved for public release; Distribution is unlimited					
<b>13. Supplementary Notes</b>					
<b>14. Abstract</b> The smoothed particle hydrodynamics (SPH) technique in conjunction with the macro-mechanics concept for fiber composites was developed to simulate impact penetration of composite structures. To describe the material behavior under high intensity loadings, a 3-D anisotropic plasticity model, an equation of state, and a failure criterion for unidirectional composites were proposed. Furthermore, to maintain material frame indifference of the constitutive equations, the polar stress rate approach was employed in the stress and strain transformation under large rotation. The above physics were incorporated into SPH. Detailed penetration process and damage progression were simulated with graphite/epoxy composite laminates impacted by a steel projectile. The predicted impact response and damage patterns agree well qualitatively with the experimental results. This study has demonstrated that SPH can be a robust and viable analytical tool for predicting response of fiber-reinforced composite structures subjected to high-velocity impact.					
<b>15. Subject Terms</b> composite laminate, impact penetration, progressive damage, smoothed particle hydrodynamics, anisotropic plasticity, equation of state, failure criterion, material frame indifference, polar stress rate					
<b>Security Classification of</b>			<b>19. Limitation of Abstract</b>  Unlimited	<b>20. # of Pages</b>  56	<b>21. Responsible Person (Name and Telephone #)</b>  Dr. Jinn-Kuen Chen 505-853-3184
<b>16. Report</b>  Unclassified	<b>17. Abstract</b>  Unclassified	<b>18. This Page</b>  Unclassified			

## CONTENTS

<u>Section</u>		<u>Page</u>
1.	EXECUTIVE SUMMARY	1
2.	INTRODUCTION	2
2.1	STATEMENT OF THE PROBLEM	2
2.2	PHYSICS OF ANISOTROPIC MATERIALS	2
3.	THEORETICAL MODEL DEVELOPMENT	4
3.1	3-D ANISOTROPIC ELASTO-PLASTICITY THEORY	4
3.1.1	MICROMECHANICS FINITE ELEMENT ANALYSIS	4
3.1.2	ANISOTROPIC YIELD FUNCTION	5
3.1.3	VERIFICATION OF THE PLASTICITY MODEL	12
3.1.4	ELASTO-PLASTIC TANGENT STIFFNESS MATRIX	12
3.2	EQUATION OF STATE	16
3.3	DYNAMIC FAILURE	18
3.4	STRESS AND STRAIN TRANSFORMATIONS	19
3.5	SMOOTHED PARTICLE HYDRODYNAMICS	23
4.	NUMERICAL RESULTS AND DISCUSSION	24
4.1	VALIDATION OF THE MODIFIED MAGI CODE	24
4.2	EFFECTS OF THE NUMBER OF PARTICLES ON SOLUTION ACCURACY	26
4.3	3-D SIMULATIONS OF COMPOSITE LAMINATE PENETRATION	26
5.	CONCLUSIONS AND RECOMMENDATION	44
6.	REFERENCES	46

## FIGURES

<u>Figure</u>		<u>Page</u>
1	A unit cell for hexagonal array	6
2	Plastic strain as a function of hydrostatic stress	7
3	Stress-strain response under uniaxial tension in the fiber direction	8
4	Master effective stress-effective plastic strain curve	11
5	Stress-strain results under simple tension in the transverse direction predicted by the micromechanics finite element model and plasticity model	13
6	Stress-strain results under uniform dilatation predicted by the micromechanics finite element model and plasticity model	14
7	Stress-strain results under tri-axial loading predicted by the micromechanics finite element model and plasticity model	15
8	Three consecutive rotations from geometry coordinate system to material coordinate system	20
9	Aluminum target and steel projectile deformation at 1.0 $\mu$ s	25
10	8-layer unidirectional composite impacted by a steel rod at 3.0 $\mu$ s, $V=2.0$ km/s (6 particles per layer)	27
11	8-layer unidirectional composite impacted by a steel rod at 3.0 $\mu$ s, $V=2.0$ km/s (2 particles per layer)	28
12	The $[0/90/45/-45]_s$ laminate impacted by a steel rod with $V=2.0$ km/s at 3.0 $\mu$ s (6 particles per layer)	29
13	The $[0/90/45/-45]_s$ laminate impacted by a steel rod with $V=2.0$ km/s at 3.0 $\mu$ s (2 particles per layer)	30
14	Penetration at different stages for the $[0/90/45/-45]_s$ laminate impacted by a steel cube with $V=2.0$ km/s	32
15	Deformation at 3.0 $\mu$ s for the $[0/90/45/-45]_s$ laminate impacted by a steel cube with $V=2.0$ km/s	33
16	Damage pattern at the cross-sections of $x=0$ , $y=0$ , and $x=y$ in the $[0/90/45/-45]_s$ laminate impacted by steel cube with $V=2.0$ km/s at 3.0 $\mu$ s	34
17	Deformation at 3.0 $\mu$ s for the $[45/-45/0/90]_s$ laminate impacted by a steel cube with $V=2.0$ km/s	35
18	Damage pattern at the cross-sections of $x=0$ , $y=0$ , and $x=y$ in the $[45/-45/0/90]_s$ laminate impacted by steel cube with $V=2.0$ km/s at 3.0 $\mu$ s	36
19	Deformation at 10.0 $\mu$ s for the $[45/-45/0/90]_s$ laminate impacted by a steel cube with $V=0.6$ km/s	37

20	A representative damage pattern in the $[45/-45/0/90]_s$ laminate impacted by a steel cube measured using C-SCAN [24]	38
21	Damage pattern at the cross-sections of $x=0$ , $y=0$ , and $x=y$ in the $[45/-45/0/90]_s$ laminate at $10.0 \mu s$ after impact by steel cube at $V=0.6 \text{ km/s}$	39
22	Deformation at $10.0 \mu s$ for the $[45/-45/0/90]_s$ laminate impacted by a steel cube at $V=0.2 \text{ km/s}$	41
23	Damage in the $[45/-45/0/90]_s$ laminate at $30.0 \mu s$ after impact by a steel cube at $V=0.2 \text{ km/s}$	42
24	Deformation of the projectiles after impact at different striking speeds	43

## 1. EXECUTIVE SUMMARY

This is the final report presented to the Survivability and Safety Branch of Wright Laboratory (WL/FIVSM). It summarizes efforts of the Satellite Assessment Division of Phillips Laboratory (PL/WSA) toward development of a high fidelity predictive structural composite penetration model. This physics based "first principle" model will be able to simulate the dynamic response and progressive damage in structural composite laminates subjected to ballistic impact of non-nuclear treats.

The need for the development of a high fidelity first principle penetration model for composite structures subjected to ballistic impact is apparent. Although the smoothed particle hydrodynamics (SPH) technique has been successfully applied to simulate hypervelocity impact of homogeneous and isotropic solid materials in the early 1990's, the need for simulating behavior of non-homogeneous, anisotropic materials under intensive dynamic loading remains. The new challenges posed by modeling the non-homogeneity and anisotropy of fiber-reinforced composites are two-fold. One is how to accurately describe anisotropic elasto-plasticity, equation of state, and failure condition for unidirectional composites under high strain-rate loadings. The other is how to feasibly implement a composite structure model in a numerical code simulation while considering the limitation of computer memory and time.

To address the former problem, PL/WSA has constructed a theoretical foundation representing the needed additional physics essentially for simulating dynamic response of composite laminates under severely elevated pressure regimes. The remaining task is to discretize and implement into the SPH the governing equations where composite laminates can be modeled numerically feasibly and economically.

Our results clearly demonstrate success in both accounts: (a) numerical simulation of composite laminate damage zone correlated well qualitatively with the known experimental data, and (b) newly improved SPH proved to be a robust and viable analytical tool for predicting response of non-homogeneous, anisotropic composite materials to intensive dynamic loadings. In conclusion, we have achieved the established goal of this task where a fundamental and economical analytical tool capable of predicting damage response of fiber-reinforced composites to impact loadings is developed. We submit however, there is a great deal more development needed before we can assess damage across a broad spectrum of composite structures. Following is a list of most pertinent topics:

- (1) generalization of the current developed anisotropic plasticity model and failure criterion for fiber-reinforced composites to encompass high strain-rate regime,
- (2) extension of the proposed equation of state for composites to include temperature and phase changes,
- (3) development of a tri-axial ellipsoidal smoothing function for prismatic particles, and
- (4) extension of the current SPH capability for interface and boundary condition applications.



## 2. INTRODUCTION

Impact damage to composite laminates has been studied extensively in the last two decades. Most efforts have been devoted to low velocity impact. Due to the constraints of technique and cost, however, relatively little progress has been achieved in the understanding of high velocity impact of laminated composites. Among the latter, Walters and Scott [1] described an experimental observation of deformation patterns within Kevlar 29® composite laminates subjected to a shaped charge jet. Brar [2] measured the force on projectile noses while penetrating composite targets as well as characterized the failure modes for S-2 Glass® composites. Other experimental efforts focused on the ballistic limit and/or residual velocity of a projectile on composite targets [3-6]. Recently, Schonberg and Walker [7] presented an experimental investigation of composite materials used as bumper shields for preventing the perforation of the pressure walls in multi-wall structural systems subjected to hypervelocity projectile impact. In the area of analytical analysis, Cantwell and Morton [8] used an energy dissipation model which accounts for elastic deformation, delamination and shear-out to predict the perforation threshold of a composite beam. This simple model predicted the experimental trends successfully only for thin laminates. Zhu et al. [9] developed a phenomenological model which comprised both global and local deformations for laminated Kevlar/polyester plates impacted by hard-steel cylindro-conical projectiles. Although an accord between the prediction and measurement of the ballistic limits, residual velocities and displacement histories of the projectile was satisfactory, it deteriorated successively when velocities and accelerations were examined. Sun and his associates [5,10] proposed a quasi-static load-displacement punch curve as the structural constitutive model for the entire perforation process. The residual velocities were then estimated based on the balance of dynamic energy. Vinson and Walker [11] extended the conical shell model for a textile flexible cloth target [12] to predict the ballistic limits and residual velocities of the impactor for fibrous polymer matrix composites. In the area of numerical analysis, Blanas [13] used the finite element code DYNA3D to evaluate ballistic limits. He concluded that DYNA3D's macromechanical model is a marginally acceptable method of modeling penetration phenomena of composite laminates only if qualitative results are needed as a structural design criterion. In an attempt to model shock wave propagation in fiber-reinforced composites, Anderson and his co-workers [14,15] modified the Mie-Gruneisen equation of state (EOS) for metals and applied it to composites so that it is able to account for the portion of the pressure resulting from deviatoric strains. The macromechanics-based anisotropic constitutive laws for composites, together with the modified EOS, were implemented into the finite difference hydrocode HEMP [14] and the finite element hydrocode EPIC [15]. Since no failure investigation was attempted, only the onset of failure can be predicted in their analyses.

The phenomena involved in high velocity impact on composite laminates are complex, including local contact, bulging, global deformation, matrix cracking, fiber breakage, fiber-matrix interface debonding, delamination, fragmentation, etc. As pointed out by Sun and Potti [10], a detailed modeling of damage progression during perforation would be a very difficult task. This is why most of the above theoretical investigations for high velocity impact on composite materials was confined to ballistic limits and residual velocities of a projectile. Recently, Chen et al. [16] have applied the SPH technique [17] to simulate the detail perforation process for B/Al composites. Since the diameter of boron fibers is relatively large as compared to the lamina thickness, they modeled the fibers and matrix as two different isotropic materials. This approach, however, is prohibitively computer memory

intensive for graphite/epoxy (Gr/Ep) composites because there is a great number of fibers over a lamina.

The new challenges posed by modeling the non-homogeneity and anisotropy of fiber-reinforced composites are two-fold. One is how to accurately describe the anisotropic elasto-plasticity, equation of state (EOS), and failure conditions for a unidirectional composite under high strain-rate loadings. The other is how to feasibly implement a composite structure model in a numerical code simulation while considering the limitation of computer memory and time.

In this report the macro-mechanics approach for fiber composites was proposed for the SPH simulations of impact penetration into Gr/Ep composites. A 3-D elasto-plasticity constitutive model, an EOS and a failure criterion which account for the anisotropic behaviors of fiber composites were developed. Since material often undergoes large rotation during impact process, stress and strain transformations between the material principal axes and the deformed configurations were also considered based on the polar stress rate approach. The above modules for fiber composites were then incorporated into the SPH.

3-D simulations were carried out with the  $[0/90/45/-45]_s$  and  $[45/-45/0/90]_s$  Gr/Ep composite laminates impacted by a steel cubic projectile. The impact velocities exceeding the ballistic limits were of interest. Detailed numerical results and comparison with the experimental data will be presented and discussed. Further development needs will also be addressed.

### 3. THEORETICAL MODEL DEVELOPMENTS

To describe the impact penetration behavior of homogeneous solid media, three conservation laws of mass, momentum and energy must be obeyed. In general, the conservation laws offer five scalar equations but involving seven unknowns which are pressure, density, internal energy, temperature, and three velocity components. In order to obtain uniqueness of the solutions, material properties, such as constitutive relationships and equations of state, will have to be imposed. Since often material would undergo large rotation during the impact process, it is also necessary to transform stresses and strains back and forth between the unrotated and deformed configurations. In addition, a strength model is needed to describe any possible fragmentation.

For a fiber rein-forced composite, the above physics are complicated and little provision has been made to account for the existing inherent non-homogeneous and anisotropic nature so far. In this section, a generalized, 3-D, anisotropic elasto-plasticity model, equation of state, and dynamic failure criterion for fiber composites will be proposed. The stress and strain transformations between the material principal coordinates and deformed configurations will be developed.

#### 3.1 ANISOTROPIC ELASTO-PLASTICITY THEORY

Several three-dimensional anisotropic plasticity models [18-24] have been proposed for fiber-reinforced composite materials. However, most of the theories suffer two shortcomings. One is that some approaches utilize the plasticity theory for metals to describe the nonlinear behavior of fiber composites. For instance, Griffin et. al [18], Hansen et. al [19], and Xie and Adams [20] employed Hill's orthotropic yield criterion. It should be noted that Hill's plasticity theory assume that hydrostatic stress does not influence plastic deformation and that the plastic dilatation is incompressible. These two assumptions are particularly questionable for fiber-reinforced composites. The other shortcoming is that some approaches do not describe material anisotropy parameters completely. The assumptions of linear elasticity in the fiber direction [20-22] and transverse isotropy [20,21,23] were commonly made. The former is acceptable only for some particular types of composites in which the elastic fibers carry the majority of load. The latter is not suitable for composites with a fiber arrangement whose overall spacings are different in the different directions. Recently, Chen et. al [24] proposed a generalized yield criterion that is quadratic in stresses for B/AI and AS4/PEEK composites. This plasticity model not only relaxes the previously imposed assumptions [18-23], but is also general in nature covering composite materials composed of various fiber arrays.

##### 3.1.1 3-D MICROMECHANICS FINITE ELEMENT ANALYSIS

Driven by laboratory testing limitations and cost, Chen et al [24] used the ANSYS code to conduct 3-D micromechanics finite element calculations to generate the nonlinear macro stress-strain data. Their micromechanics model was based on a representative volume element (RVE) or unit cell. The analysis was performed under the assumption that the periodic fiber arrangement is in the form of square array.

In reality, however, in a composite lamina the fiber distribution is not regular within the cross-section. As reported by Sun and Vaidya [25], for the AS4/PEEK composite a hexagonal array gives a better prediction of the nonlinear behavior of the composite than a square array. In the present 3-D micromechanics finite element analysis, thus, the hexagonal array is employed for the nonlinear stress-strain data acquisition. The composite system considered here is the AS4/3501-6 with 66% fiber volume

ratio (Fig. 1). The fibers are assumed to be transversely isotropic and linearly elastic. The matrix exhibits elastic-plastic characteristics and obeys the von Mises  $J_2$  flow rule. The elastic constants used in the numerical analysis are given as follows:

AS4 fiber:	$E_{11} = 234 \text{ GPa},$	$E_{22} = E_{33} = 13.8 \text{ GPa},$
	$G_{23} = 5.5 \text{ GPa},$	$G_{12} = G_{13} = 27.6 \text{ GPa},$
	$\nu_{23} = 0.25,$	$\nu_{12} = \nu_{13} = 0.2;$
3501-6 epoxy:	$E = 4.8 \text{ GPa},$	$\nu = 0.34.$

The nonlinear uniaxial stress-strain curve for the 3501-6 epoxy can be found in Adams and Crane [26]. The finite element model, load and boundary conditions applied to the RVE are described in [24]. The numerical analysis was carried out using the ANSYS code.

Figure 2 shows the predicted macro plastic strains in the AS4/3501-6 composite lamina subjected to hydrostatic stress. The stress-strain responses are the same in both the transverse directions. It is clear that the sum of three normal plastic strain components is not zero. This reveals that for the AS4/3501-6 composite hydrostatic pressure not only influences plastic deformation, but the plastic dilatation is compressible as well. The stress-strain curves under uniaxial simple tension loading in the fiber direction are plotted in Fig. 3. The solid lines are the linearly elastic solutions, and the circles present the elastic-plastic solutions. At 1% of the total longitudinal strain, for example, the plastic strain component is about 0.35% of the total strain. The contraction in the transverse directions at this load is about 0.2%. The plastic strain portion is about 7.3% of the total contraction. If the assumption of linear elasticity in the fiber direction is posed in developing an anisotropic plasticity model, then these plastic deformations will vanish. It is recommended, in the interest of more accurate solution, that the imposed assumption be removed.

### 3.1.2 ANISOTROPIC YIELD FUNCTION

The generalized, 3-D anisotropic yield function proposed by Chen et al. [24] is given as,

$$\begin{aligned}
 f(\sigma_{ij}) = & a_{11}\sigma_{11}^2 + a_{22}\sigma_{22}^2 + a_{33}\sigma_{33}^2 + 2a_{12}\sigma_{11}\sigma_{22} + 2a_{23}\sigma_{22}\sigma_{33} \\
 & + 2a_{13}\sigma_{11}\sigma_{33} + 2a_{44}\sigma_{23}^2 + 2a_{55}\sigma_{31}^2 + 2a_{66}\sigma_{12}^2 \\
 = & k
 \end{aligned} \tag{1}$$

where the stresses  $\sigma_{ij}$  refer to the principal material directions, and  $k$  is a state variable. The nine plasticity coefficients  $a_{ij}$  describe the amount of anisotropy in plasticity. This yield criterion reduces to the Hill's orthotropic yield function when

$$\begin{aligned}
 a_{12} &= a_{33} - (a_{11} + a_{22} + a_{33})/2 \\
 a_{13} &= a_{22} - (a_{11} + a_{22} + a_{33})/2 \\
 a_{23} &= a_{11} - (a_{11} + a_{22} + a_{33})/2
 \end{aligned} \tag{2}$$

Assuming the associated flow rule, the incremental plastic strains  $d\epsilon_{ij}^p$  can be written as

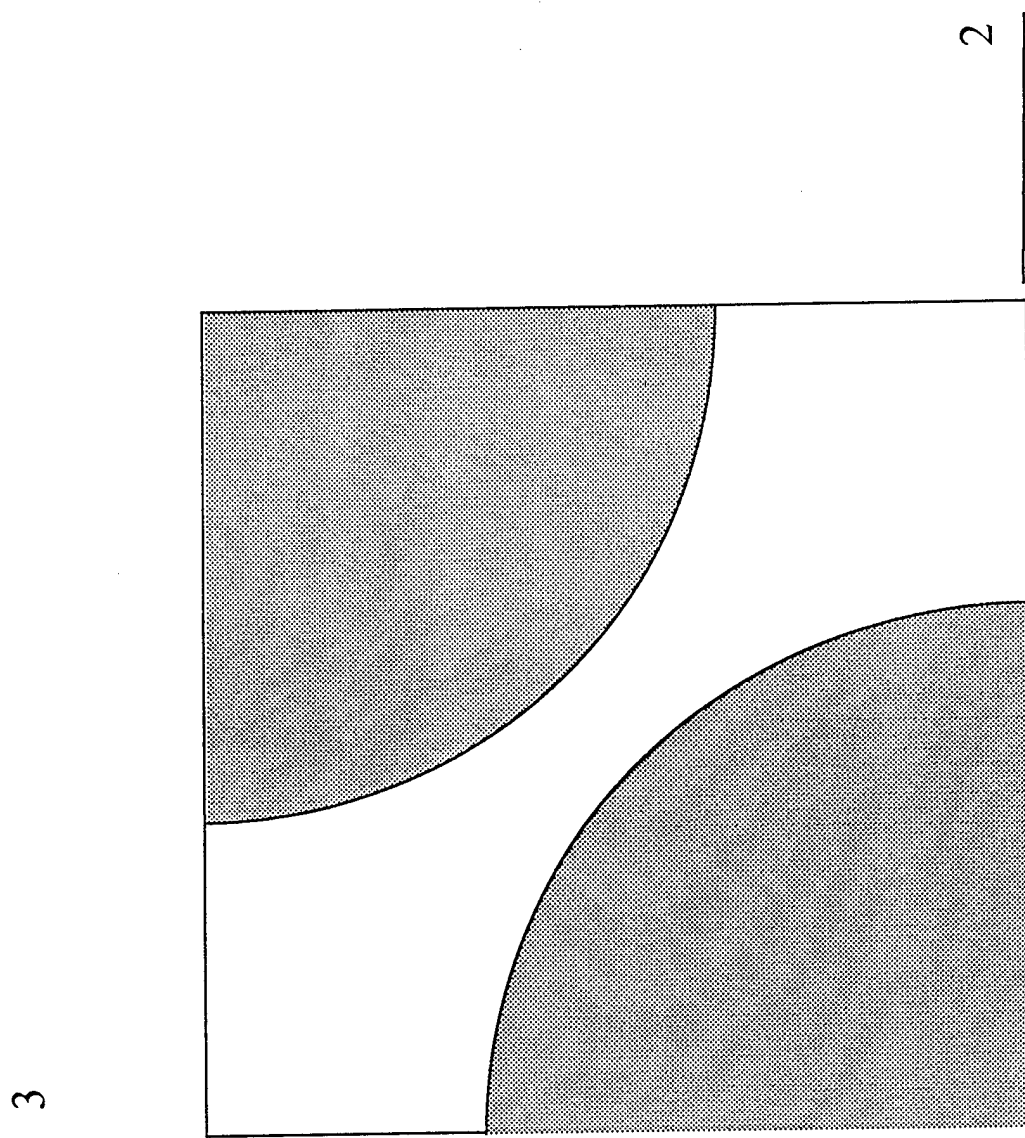


Fig. 1 A unit cell for hexagonal array

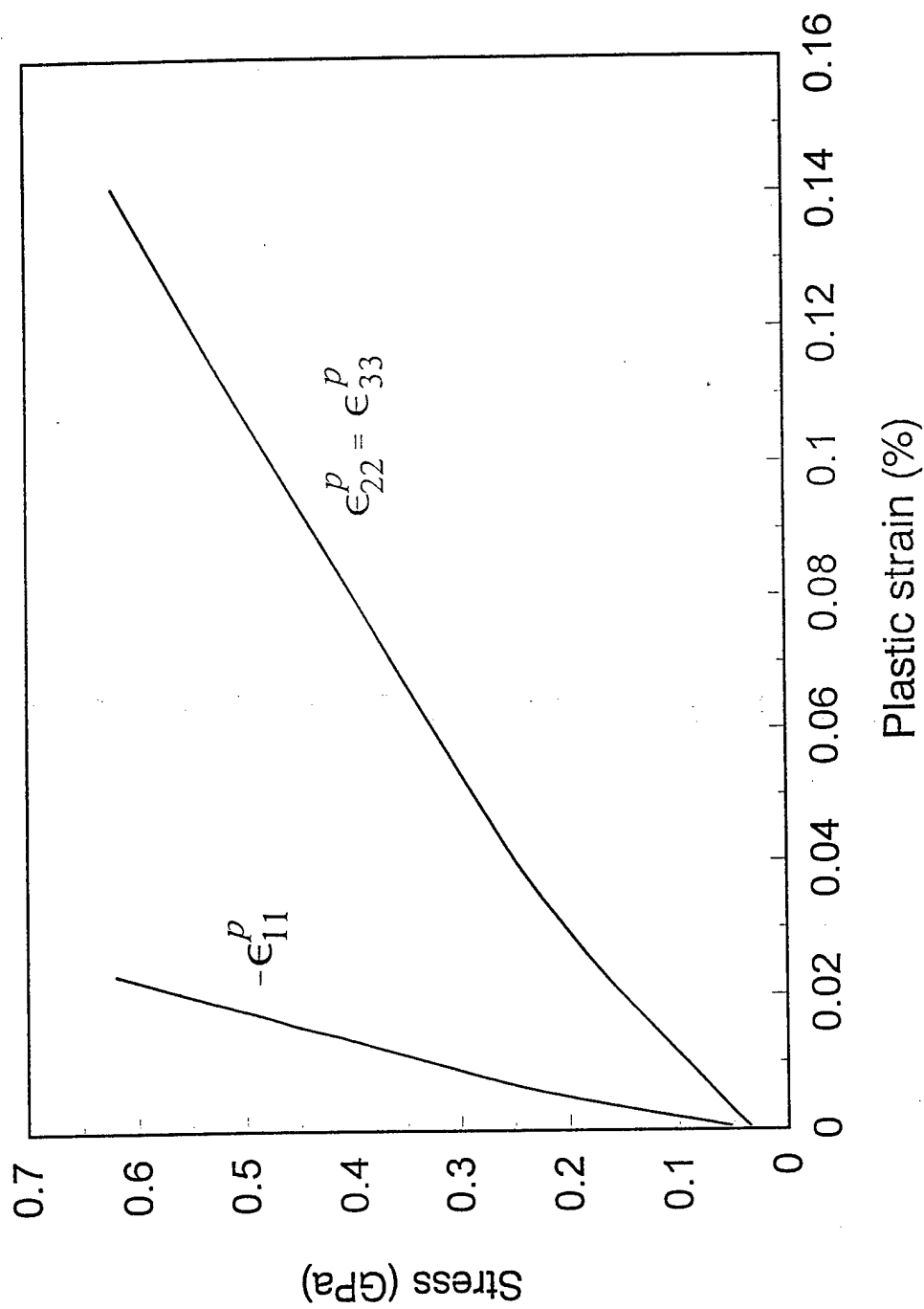


Fig. 2 Plastic strain as a function of hydrostatic stress

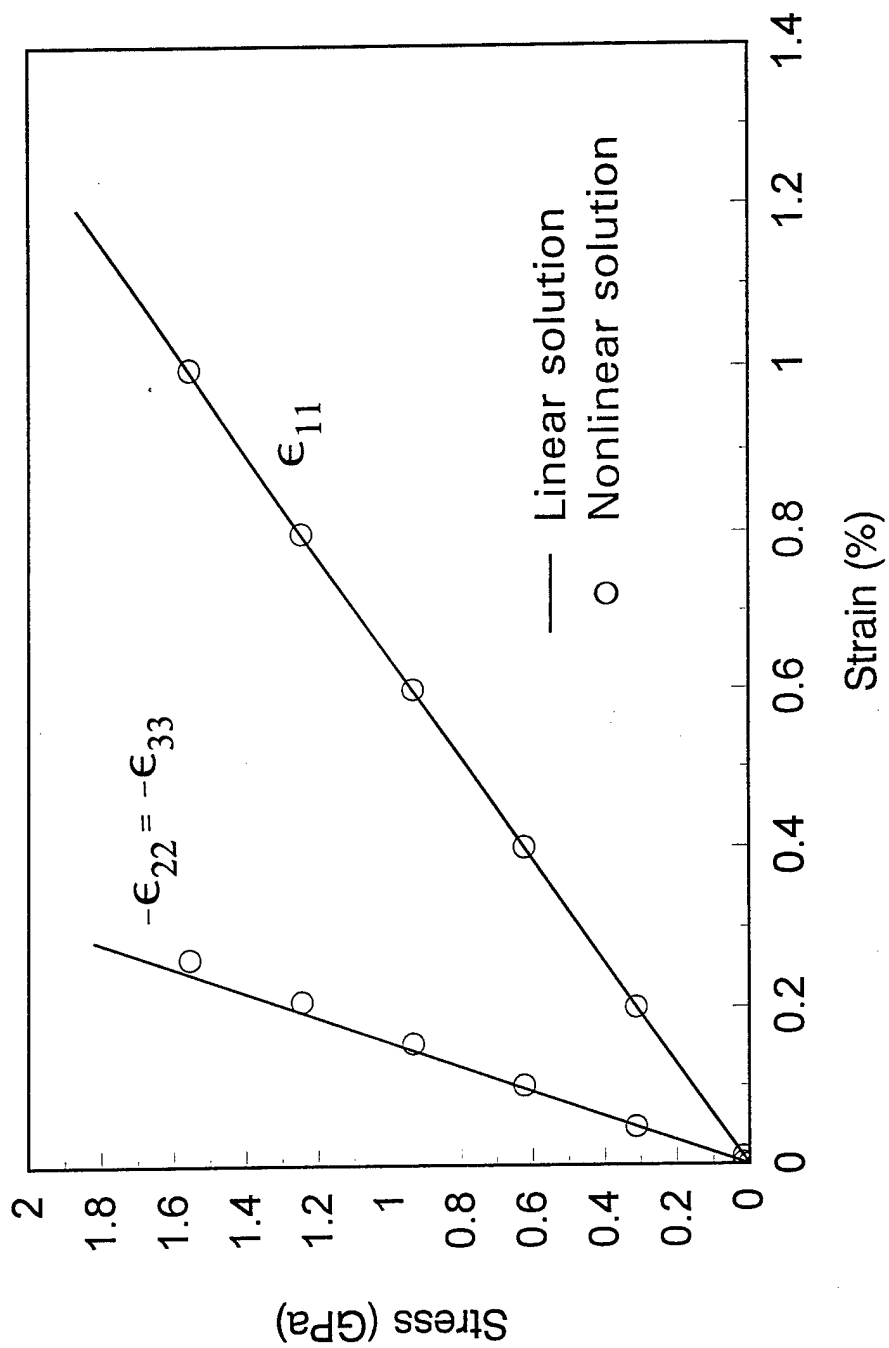


Fig. 3 Stress-strain response under uniaxial tension in the fiber direction

$$d\epsilon_{ij}^p = d\lambda \frac{\partial f}{\partial \sigma_{ij}} \quad (3)$$

in which the superscript  $p$  denotes plasticity, and  $d\lambda$  is a plastic factor. Let the effective stress  $\bar{\sigma}$  be defined as

$$\bar{\sigma} = \sqrt{\frac{3}{2}f} \quad (4)$$

By comparing Eqs. (1) and (4), one finds that

$$k = \frac{2}{3}\bar{\sigma}^2 \quad (5)$$

The incremental effective plastic strain  $d\bar{\epsilon}^p$  can be derived through the concept of plastic work:

$$dW^p = \sigma_{ij} d\epsilon_{ij}^p = \bar{\sigma} d\bar{\epsilon}^p \quad (6)$$

From Eqs. (1), (3) and (6), thus, the incremental effective plastic strain can be expressed as

$$d\bar{\epsilon}^p = \frac{4}{3}\bar{\sigma} d\lambda \quad (7)$$

Substituting Eq. (1) into (7) with the inversion of Eq. (3) for  $\sigma_{ij}$  and regrouping it yields  $d\bar{\epsilon}^p$  in an explicit form

$$\begin{aligned} (d\bar{\epsilon}^p)^2 = & \frac{2}{3\Delta} \left\{ A_{11}(d\epsilon_{11}^p)^2 + A_{22}(d\epsilon_{22}^p)^2 + A_{33}(d\epsilon_{33}^p)^2 + 2A_{12}d\epsilon_{11}^p d\epsilon_{22}^p + 2A_{23}d\epsilon_{22}^p d\epsilon_{33}^p + 2A_{13}d\epsilon_{11}^p d\epsilon_{33}^p \right\} \\ & + \frac{4}{3} \left\{ \frac{(d\epsilon_{23}^p)^2}{a_{44}} + \frac{(d\epsilon_{31}^p)^2}{a_{55}} + \frac{(d\epsilon_{12}^p)^2}{a_{66}} \right\} \end{aligned} \quad (8)$$

where

$$\Delta = \begin{vmatrix} a_{11} & a_{12} & a_{13} \\ a_{12} & a_{22} & a_{23} \\ a_{13} & a_{23} & a_{33} \end{vmatrix} \quad (9)$$

and

$$\begin{aligned} A_{11} &= a_{22}a_{33} - a_{23}^2, & A_{22} &= a_{11}a_{33} - a_{13}^2, & A_{33} &= a_{11}a_{22} - a_{12}^2 \\ A_{12} &= a_{13}a_{23} - a_{12}a_{33}, & A_{13} &= a_{12}a_{23} - a_{13}a_{22}, & A_{23} &= a_{12}a_{13} - a_{11}a_{23} \end{aligned} \quad (10)$$

The determinant in Eq. (9) is zero for a material which obeys the von Mises flow rule or the Hill criterion because of the condition of the incompressibility of plastic dilatation.

The  $\bar{\sigma}$ - $\bar{\epsilon}^p$  relationship for a particular loading can then be obtained from Eqs. (1), (3), (4) and (8). For example, consider a uniaxial loading,  $\sigma_{ii} \neq 0$  only (no summation). By using Eqs. (1) and (4), the effective stress becomes



$$\bar{\sigma} = \sqrt{\frac{3a_{ii}}{2}} \sigma_{ii} \quad (11)$$

The incremental plastic strain components, Eq. (3), can be written as

$$d\epsilon_{jj}^p = \frac{a_{ji}}{a_{ii}} d\epsilon_{ii}^p, \quad d\epsilon_{kk}^p = \frac{a_{ik}}{a_{ii}} d\epsilon_{ii}^p, \quad d\epsilon_{ij}^p = 0 \quad (i \neq j) \quad (12)$$

Substitution of Eq. (12) into (8) yields the incremental effective plastic strain,

$$d\bar{\epsilon}^p = \sqrt{\frac{2}{3a_{ii}}} d\epsilon_{ii}^p \quad (13)$$

The incremental effective plastic strain can also be derived by substituting (11) into (7) and utilizing (3).

For a shear loading,  $\sigma_{ij} \neq 0$  only, the effective stress becomes

$$\bar{\sigma} = \sqrt{3a_{rr}} \sigma_{ij} \quad (14)$$

where  $rr = 44, 55$  or  $66$  depending upon the shear stress component (see Eq. 1). The incremental effective plastic strain is then given as

$$d\bar{\epsilon}^p = \frac{2d\epsilon_{ij}^p}{\sqrt{3a_{rr}}} \quad (15)$$

In principle, a master  $\bar{\sigma}$ - $\bar{\epsilon}^p$  relationship for a unidirectional composite can be defined with any of the three normal stress-strain curves and three shear stress-strain data, using either Eqs. (11) and (13) or Eqs. (14) and (15). In this study, the macro stress-strain response in the 2-direction together with setting  $a_{22} = 1.0$ , without loss of generality, was considered to define the master  $\bar{\sigma}$ - $\bar{\epsilon}^p$  curve. Once the master  $\bar{\sigma}$ - $\bar{\epsilon}^p$  curve for the composite is obtained, the values of  $a_{11}$ ,  $a_{33}$ ,  $a_{44}$ ,  $a_{55}$  and  $a_{66}$  can be chosen by the trial and error optimization such that all five stress-strain curves are brought into coincidence with the master  $\bar{\sigma}$ - $\bar{\epsilon}^p$  curve. The other constants associated with the interaction between any two normal stresses,  $a_{12}$ ,  $a_{13}$  and  $a_{23}$ , can be approximated using Eq. (12). The detail of the calibration procedure can be found in Ref. 9.

Using the predicted macro stress-strain data from the micromechanics finite element analysis, the nine plasticity parameters in the anisotropic yield function (Eq. (1)) for the AS4/3501-6 composites are calibrated as follows:

$$\begin{aligned} a_{11} &= 0.00058, & a_{22} &= a_{33} = 1.0, \\ a_{23} &= -0.975, & a_{12} &= a_{13} = -0.0025 \\ a_{44} &= 0.58, & a_{55} &= a_{66} = 1.45. \end{aligned}$$

The corresponding master effective stress-effective plastic strain curve is shown in Fig. 4.

### 3.1.3 VERIFICATION OF THE PLASTICITY MODEL

The verification of the anisotropic plasticity model established for the AS4/3501-6 composite was

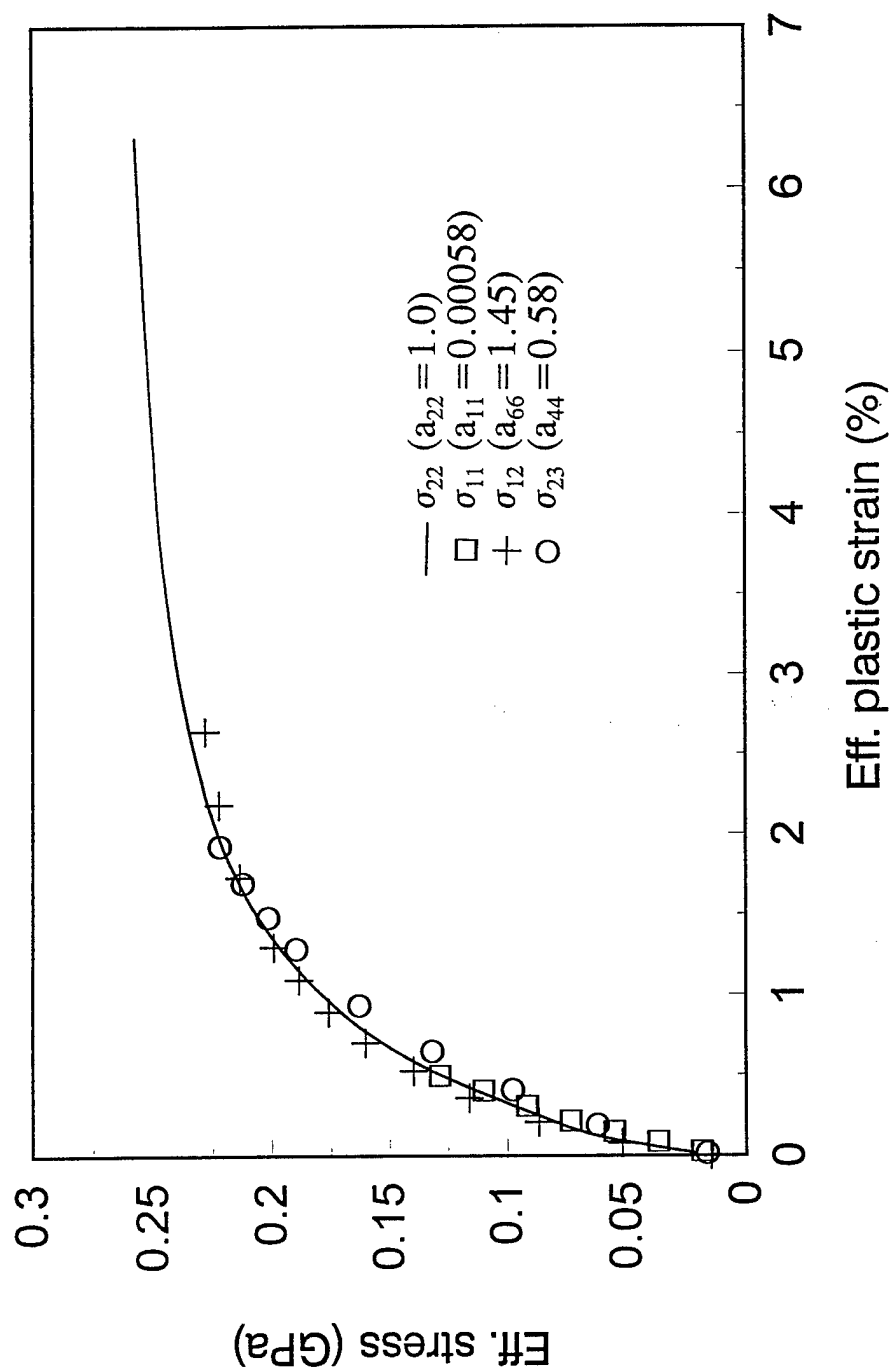


Fig. 4 A master effective stress-effective plastic strain curve

conducted with the three cases: (1) uniaxial tension in the 2-direction, (2) uniform dilatation, and (3) a tri-axial stress case with the loading ratio 10:1:-2. The effective moduli used in the verifications are predicted from the 3-D micromechanics finite element model and are given as follows:

$$\begin{aligned} E_{11} &= 156 \text{ GPa}, & E_{22} &= E_{33} = 9.28 \text{ GPa}, \\ G_{23} &= 3.78 \text{ GPa}, & G_{12} &= G_{13} = 7.36 \text{ GPa}, \\ \nu_{23} &= 0.389, & \nu_{12} &= \nu_{13} = 0.244. \end{aligned}$$

Figures 5 shows the comparison of the total stress and strain results predicted by the 3-D micromechanics finite element model and the anisotropic plasticity mode for the uniaxial tension in the 2-direction. The agreement between the two results is excellent. At  $\sigma_{22} = 0.209 \text{ GPa}$ , the relative errors are 1.6% for  $\epsilon_{22}$  and 0.9% for  $\epsilon_{33}$ . The uniform dilatation case is presented in Fig. 6. As seen in the figure, the solutions predicted by the plasticity model match very well with those predicted by the 3-D micromechanics finite element model. It is interesting to note that the plasticity in this case is insignificant. Figures 7 shows the comparison of the total stress and strain results for the tri-axial stress case. Again, there is an excellent agreement between both predictions. At the maximum load calculated here, the relative errors are 2.4% for  $\epsilon_{11}$ , 2.1% for  $\epsilon_{22}$ , and 1.1% for  $\epsilon_{33}$ .

### 3.1.4 ELASTO-PLASTIC TANGENT STIFFNESS MATRIX

With the confidence of the anisotropic plasticity model, the elastic-plastic constitutive relationship will be established. The plastic factor  $d\lambda$  can be determined by rewriting Eq. (7)

$$d\lambda = \frac{3}{4} \frac{d\bar{\sigma}}{H_p \bar{\sigma}} \quad (16)$$

in which  $H_p \equiv d\bar{\sigma} / d\bar{\epsilon}^p$  is the slope of the master  $\bar{\sigma}-\bar{\epsilon}^p$  curve.

If the incremental strains  $d\epsilon_{ij}$  are small, one is able to linearly decompose them into the elastic part  $d\epsilon_{ij}^e$  and the plastic part  $d\epsilon_{ij}^p$  as

$$d\epsilon_{ij} = d\epsilon_{ij}^e + d\epsilon_{ij}^p \quad (17)$$

The elastic strain increment is defined by the linearly elastic constitutive relationship

$$\{d\epsilon^e\} = [S^e] \{d\sigma\} \quad (18)$$

where  $[S^e]$  is the elastic compliance matrix, and  $\{d\sigma\}$  is the incremental stress vector. From Eqs. (3) and (16), one has the relations between the incremental plastic strains and the incremental stresses as

$$\{d\epsilon^p\} = [S^p] \{d\sigma\} \quad (19)$$

where  $[S^p]$  is the plastic compliance matrix. The entities of  $[S^p]$  are obtained by substituting Eqs. (1), (4) and (16) for  $f$ ,  $d\bar{\sigma}$ , and  $d\lambda$ , respectively, into Eq. (3). They are

$$S_{ij}^p = \mu C_i C_j \quad i, j = 1, 2, \dots, 6 \quad (20)$$

in which

$$C_i = \frac{\partial f}{\partial \sigma_i}; \quad \mu = \frac{9}{4} \frac{1}{\bar{\sigma}^2} \frac{1}{H_p} \quad (21)$$

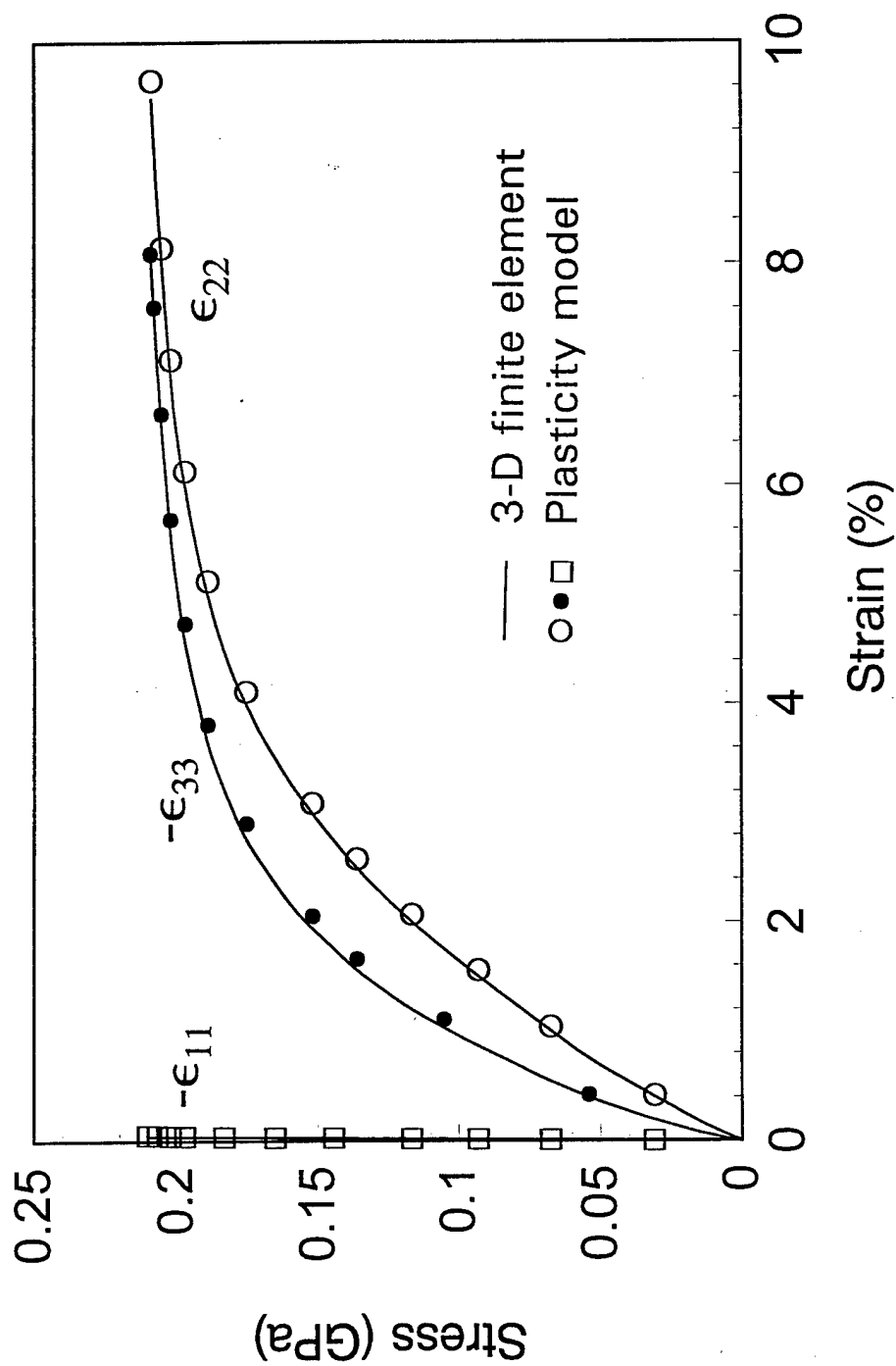


Fig. 5 Stress-strain results under simple tension in the transverse direction predicted by the micromechanics finite element model and plasticity model

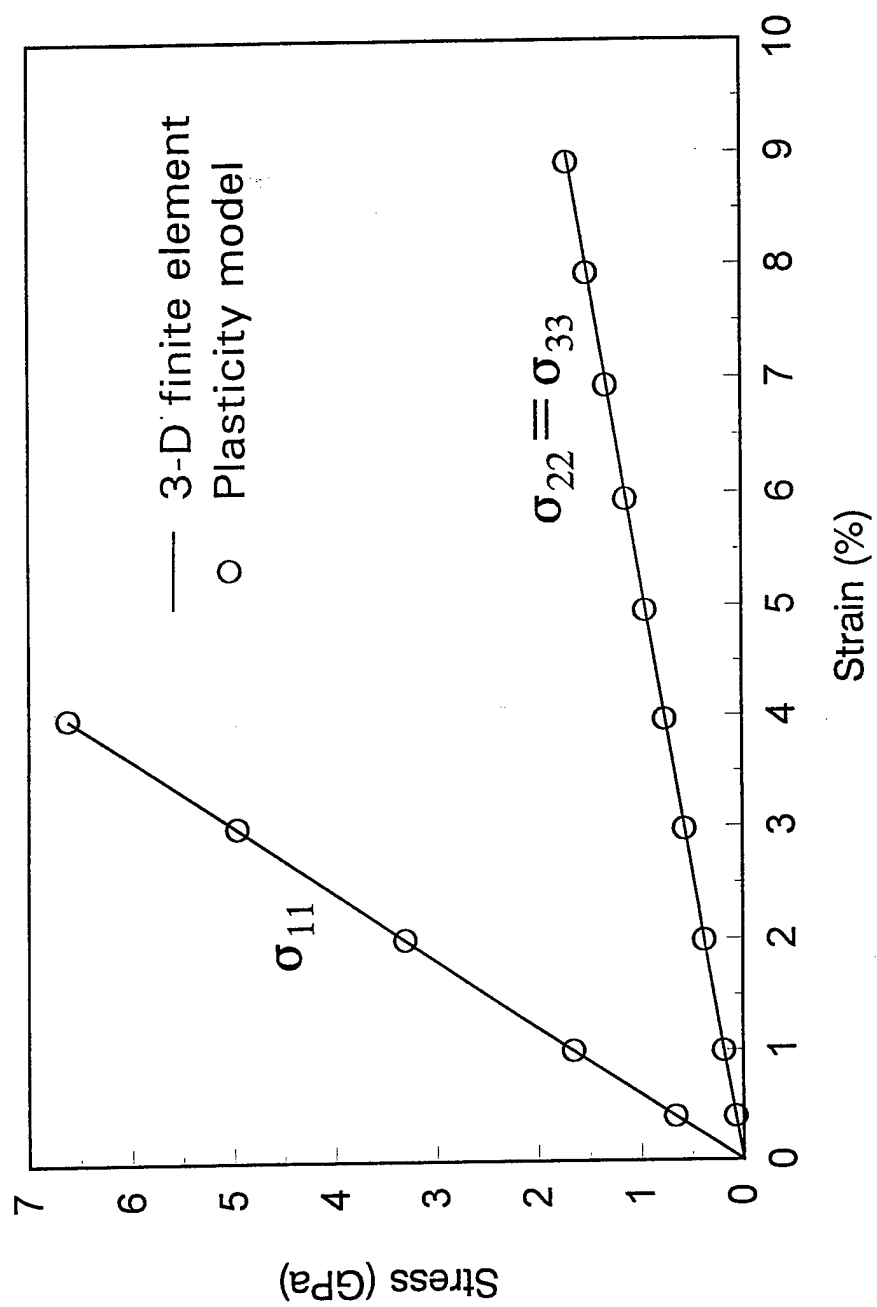


Fig. 6 Stress-strain results under uniform dilatation predicted by the micromechanics finite element model and plasticity model

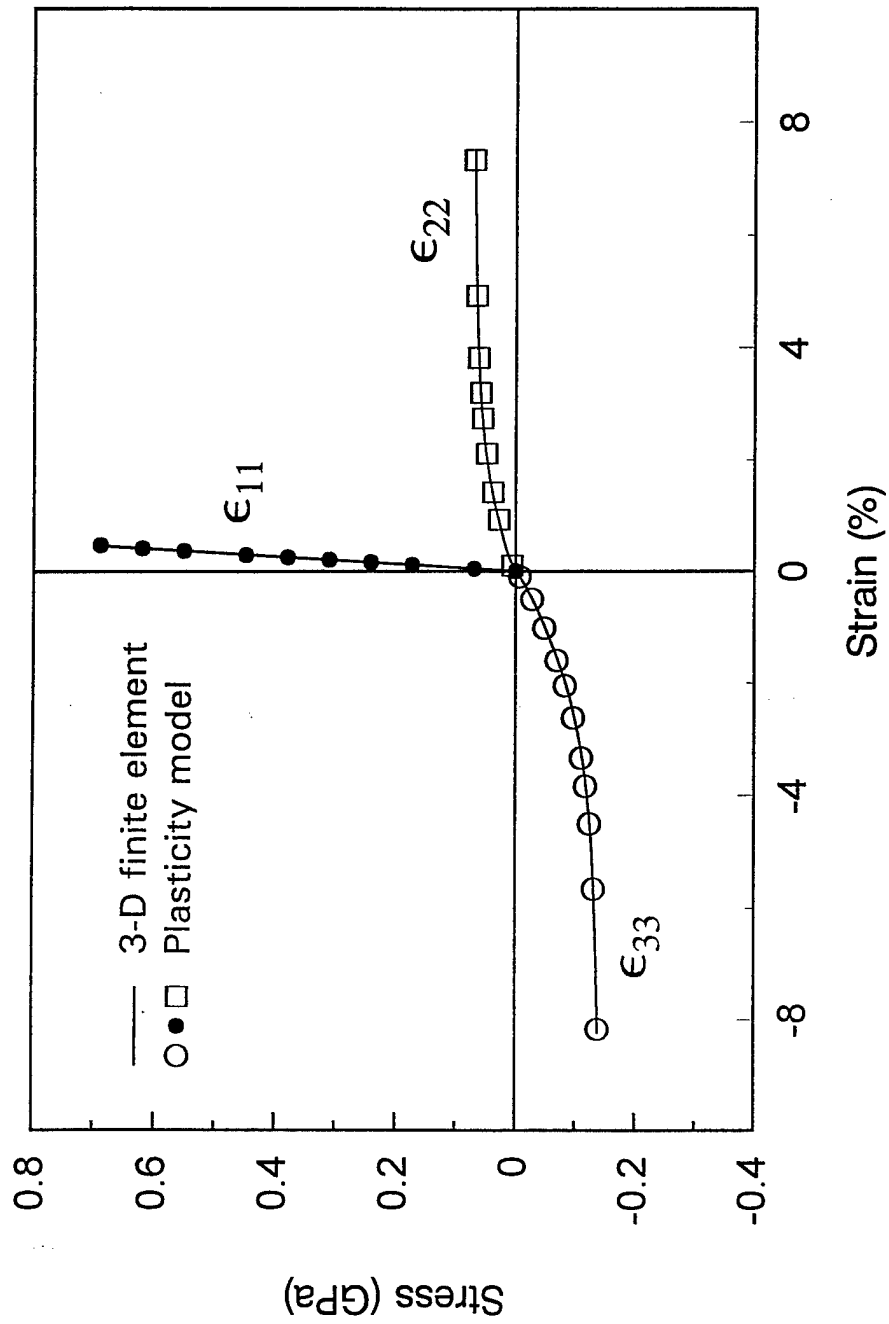


Fig. 7 Stress-strain results under tri-axial loading predicted by the micromechanics finite element model and plasticity model

where the subscript  $i$  for  $\sigma$ : 1=11, 2=22, 3=33, 4=23, 5=31, and 6=12. The relations of the complete elastic-plastic stress increments  $d\sigma_{ij}$  and the total strain increments  $d\epsilon_{ij}$  are then derived:

$$\{d\sigma\} = [D^{ep}] \{d\epsilon\} \quad (22)$$

where the elastic-plastic tangent stiffness matrix is

$$[D^{ep}] = ([S^e] + [S^p])^{-1} \quad (23)$$

Equation (22) can uniquely determine the elasto-plastic stress changes  $\{d\sigma\}$  which arise during any iteration in which known, finite changes of strain  $\{d\epsilon\}$  are imposed.

To calculate the elasto-plastic stresses, the scaling factor approach [27] is employed. At each time step, a trial stress state is first computed with the assumption of elastic deformation. If the loading surface is violated by the elastic trial stresses, then the stresses will be bring back to the yield surface from the overshooting stress state. In this study, the portion of the strain increment corresponding to the stress increment beyond the yield value is divided into 5 sub-intervals. The final stresses are determined by summing the stresses on the yield surface and the elasto-plastic stress increments sequentially calculated five times, using Eq. (22) with the updated plastic compliance matrix  $[D^{ep}]$  each time.

### 3.2 EQUATION OF STATE

For metal materials, plastic flow is often assumed to not be influenced by hydrostatic pressure. Thus, stresses are split into two parts, i.e., hydrostatic pressure and deviatoric stresses. The hydrostatic pressure  $p$  is then calculated using an equation of state (EOS) having the functional form  $p = p(\rho, e)$ .

For a fiber-reinforced composite, both the classical assumptions used in the Hill's orthotropic yield function are questioned as shown in Fig. 2. Thus, the application of the conventional approach in which the total stresses are partitioned into hydrostatic pressure and deviatoric stresses to fiber-reinforced composites remains a challenge.

Recently, Anderson et. al [15] proposed a modified version of the Mie-Gruneisen EOS for fiber composites. The pressure used in their EOS is still defined as the negative of the average of the three normal stress components. Therefore, the modified EOS must account for the portion of the pressure resulting from the deviatoric strains, which is evaluated based on the linear elasticity assumption. The credibility of this EOS was not validated yet, especially the linear elasticity correction for the deviatoric strains.

It is interesting to notice the results shown in Fig. 6 for the AS4/3501-6 composite under uniform dilatation. Although some plasticity exists in the composite, it is much less pronounced as compared with that under hydrostatic stress (Fig. 2). Therefore, the assumption that uniform dilatation does not influence plastic deformation a better approximation for the AS4/3501-6 composites. With this assumption, it may be convenient to define the "pressure" as the negative of the average of the three normal stress components only corresponding to the volumetric strain. Then this "pressure" can be computed using the Mie-Gruneisen EOS without any modifications. Once the "pressure" change between two consecutive time steps is determined, the three normal stress components corresponding to the change of uniform dilatation can be retrieved using the linearly elastic relationship. The total trial stress increments are then evaluated by summing the normal stress changes and the elastic "deviatoric" stress increments which are associated only with the deviatoric strains. Then the scaling factor algorithm

mentioned previously is employed to compute the elasto-plastic stresses. Note that the "pressure" introduced here is different from the hydrostatic pressure defined by Anderson et al [15].

The Mie-Gruneisen EOS is a theoretically sound model for crystalline metals. It is suitable for high (but not extremely high) velocity impact events [28]. The Mie-Gruneisen EOS is given as:

$$p(\rho, e) = (1 - \frac{1}{2}\Gamma\eta)p_H(\rho) + \Gamma\rho e \quad (24)$$

where  $\Gamma$  is the Gruneisen constant of the material,  $\eta = \rho/\rho_0 - 1$  represents the compressive behavior, and  $p_H(\rho)$  is the so-called Hugoniot curve which represents the locus of all points that may be reached by a shock transition from an initial unshocked state  $(p_0, \rho_0)$ . Several forms of the Hugoniot have been proposed. The one commonly used in SPH is written as

$$p_H = \begin{cases} a_1\eta + a_2\eta^2 + a_3\eta^3 & \eta > 0 \\ a_1\eta & \eta < 0 \end{cases} \quad (25)$$

The coefficients  $a_1$ ,  $a_2$ , and  $a_3$  in Eq. (25) are obtained from experimental shock compression data. Alternatively, they are analytically determined through a Taylor's series expansion of the Hugoniot curve  $p_H = c^2\eta(1+\eta)/[1-\eta(\xi-1)^2]$  as follows [17]:

$$\begin{aligned} a_1 &= \rho_0 c^2 \\ a_2 &= a_1[1 + 2(\xi - 1)] \\ a_3 &= a_1[2(\xi - 1) + 3(\xi - 1)^2] \end{aligned} \quad (26)$$

in which  $\xi$  is the constant in the approximated linear relationship between the shock velocity ( $u_s$ ) and particle velocity ( $u_p$ ),

$$u_s = c + \xi u_p \quad (27)$$

Since the sound speeds are different in the three directions for fiber composites, an equivalent (bulk) sound speed  $c$  used in Eqs. (26) and (27) will be proposed. For a fiber composite, the linear bulk modulus  $\bar{\kappa}$  evaluated based on the uniform dilatation condition is given as

$$\bar{\kappa} = \frac{1}{9\Delta} \left\{ \frac{1 - \nu_{23}\nu_{32}}{E_{22}E_{33}} + \frac{1 - \nu_{13}\nu_{31}}{E_{11}E_{33}} + \frac{1 - \nu_{12}\nu_{21}}{E_{11}E_{22}} + 2 \left( \frac{\nu_{21} + \nu_{31}\nu_{23}}{E_{22}E_{33}} + \frac{\nu_{31} + \nu_{21}\nu_{32}}{E_{22}E_{33}} + \frac{\nu_{12} + \nu_{12}\nu_{31}}{E_{11}E_{11}} \right) \right\} \quad (28)$$

Equation (28) can be simplified for isotropic materials as,

$$\kappa = \frac{E}{3(1-2\nu)} \quad (29)$$

The equivalent (bulk) Poisson's ratio for the composite is assumed to be

$$\bar{\nu} = \nu_f V_f + \nu_m (1 - V_f) \quad (30)$$

Thus, the equivalent sound speed  $\bar{c}$  for the composite can be determined using the relationship from isotropic materials

$$\bar{c} = \sqrt{\frac{\bar{E}(1-\bar{\nu})}{(1+\bar{\nu})(1-2\bar{\nu})\bar{\rho}}} \quad (31)$$

where  $\bar{\rho}$  is the density of the composite, and  $\bar{E}$  is the equivalent Young's modulus of the composite and



is evaluated using Eq. (29) with the bulk modulus and equivalent Poisson's ratio.

The constants,  $\Gamma$  and  $\xi$ , and the bulk sound speed for the AS4/3506-1 composite used in the EOS calculation are set as follows:  $\Gamma = 0.87$ ,  $\xi = 1.57$ , and  $\bar{c} = 4.69$  km/s.

It is important to note that the proposed Mie-Gruneisen EOS for anisotropic materials as well as the determination of the constants  $a_1$ ,  $a_2$ , and  $a_3$  using Eq. (26) should be validated experimentally. In this study, the "pressure" was computed using the EOS for updating the shock speed. It was not used in the stress calculation.

### 3.3. DYNAMIC FAILURE

The theoretical investigation for detail dynamic damage in composite structures due to high velocity impact is very limited. One of the main reasons is lack of a high fidelity rate-dependent failure criterion. Recently, Randles and Memes [29] proposed a continuum damage model for thick quasi-isotropic laminates based on the assumption of homogenous, transversely isotropic behavior for both stiffness and damage. They also demonstrated a good prediction of delamination type damage and spallation under uniaxial strain condition [30]. It should be noted that the approximation of transverse isotropy is suitable only for stiffness. Once local damage occurs, the initial quasi-isotropic laminate will lose its transversely isotropy. Therefore, the capability of their continuum damage model for detailed, 3-D damage predictions should further be verified.

To predict detailed damage in a fiber composite, using a layer-wise damage model in the SPH could be a more practical approach. Since it is still not available so far, a modified maximum stress failure criterion is employed for the dynamic failure analysis in this study. Fracture of a particle is said to have occurred if any tensile stress or shear stress in principal material directions is greater than or equal to the corresponding strength,

$$\begin{aligned}\sigma_{11} &\geq X_t \\ \sigma_{22} &\geq Y_t \\ |\sigma_{12}| &\geq S_{12} \\ |\sigma_{13}| &\geq S_{13} \\ |\sigma_{23}| &\geq S_{23}\end{aligned}\tag{32}$$

where  $X_t$  and  $Y_t$  are the tensile strengths in the fiber and transverse directions, respectively, and  $S_{ij}$  are the shear strengths. When any one of the inequalities in Eq. (32) is satisfied, the particle is assumed to instantaneous fail in the respective mode. Once it happens, the material can no longer support the corresponding tensile and shear loads. For instance, if  $\sigma_{11} > X_t$ , then  $\sigma_{11} = \sigma_{12} = \sigma_{13} = 0$ . If  $|\sigma_{23}| > S_{23}$ , then  $\sigma_{23} = 0$ ,  $\sigma_{22} = 0$  if  $\sigma_{22} > 0$ , and  $\sigma_{33} = 0$  if  $\sigma_{33} > 0$ . No compressive failure is assumed.

In reality, dynamic fracture strengths depend on strain rate, temperature, and/or other factors. Therefore, a range of rate-dependent stress-strain curves would be necessary to apply for simulating a high rate interaction event. However, it is difficult, technically, to obtain a full range of temperature- and rate-dependent material properties, especially for the strain rate beyond  $10^5$  cm/cm-s. For simplicity, only one value was assigned for each strength in this study. Because of the ductile behavior in the epoxy resin, the dynamic transverse strength and shear strengths of the composite were assumed to be five times the static strengths. On the other hand, the dynamic longitudinal strength remained its static value

since the plasticity in the fiber direction is much insignificant. Thus, the values of the dynamic strengths for the AS4/3501-6 composite used in this study are:  $X_t = 1.447$  GPa,  $Y_t = 0.26$  GPa, and  $S_{12} = S_{13} = S_{23} = 0.465$  GPa.

### 3.4 STRESS AND STRAIN TRANSFORMATIONS

In the analysis of composite laminate penetration, factors which contribute to misalignment of the global geometry coordinate system (GGCS) and material coordinate system (MCS) include initial layups and large rotation which material experiences during the penetration process. It is convenient to evaluate stresses in the MCS and then transform them back to the GGCS for displacement and subsequent strain calculations. Therefore, it is necessary to trace the principal material axes and transform stresses and strains back and forth between the GGCS and MCS, during the entire solution course. In doing that, the Green-Naghdi stress rate approach was adopted because it is superior to the Jaumann stress rate approach. Our transformation algorithm for fiber composites is extended from the scheme of Flanagan and Taylor [31] which was developed for isotropic materials.

Let the GGCS and MCS be two sets of rectangular Cartesian coordinates. The rotation between these two systems can be specified by the three Euler angles (Fig. 8). The individual transformation matrices for the three consecutive rotations are anti-symmetric and can easily be derived. The transformation matrix for the initial material layups,  $[R]_{om}$ , which is from the original (fixed reference) GGCS ( $x_o, y_o, z_o$ ) to the MCS ( $x_3, y_3, z_3$ ), is the chain-product of the three individual transformation matrices and is given as

$$[R]_{om} = \begin{bmatrix} c_1 c_3 - s_1 c_2 s_3 & -c_1 s_3 - s_1 c_2 c_3 & s_1 s_2 \\ s_1 c_3 + c_1 c_2 s_3 & c_1 c_2 c_3 - s_1 s_3 & -c_1 s_2 \\ s_2 s_3 & s_2 c_3 & c_2 \end{bmatrix} \quad (33)$$

where  $c_i = \cos\theta_i$ ,  $s_i = \sin\theta_i$ , and  $\theta_i$  is the  $i$ -th Euler angle.

Let  $[F]$  be the deformation gradient. Applying the polar decomposition theorem to  $[F]$  yields

$$[F] = [V][R]_{ox} = [R]_{ox}[U] \quad (34)$$

where  $[V]$  and  $[U]$  are the left- and right-symmetric stretch tensors, respectively, and  $[R]_{ox}$  is an orthogonal, material rotation tensor. The second part of Eq. (34),  $[R]_{ox}[U]$ , may be viewed as deformation being first purely stretched from the reference configuration to an unrotated configuration and then purely rotated from the unrotated configuration to the current configuration. The first part,  $[V][R]_{ox}$ , may be viewed as deformation being rotated from the reference configuration to an rotated configuration and then stretched from the rotated configuration to the current configuration. Thus,  $[U]$  is the stretch referred to the reference GGCS and  $[V]$  the rotated frame.

The velocity gradient denoted by  $[L]$  may be expressed in terms of  $[F]$  as

$$[L] = [\dot{F}][F]^{-1} \quad (35)$$

where the superposed dot indicates the time derivative and the superscript "-1" denotes the inverse of

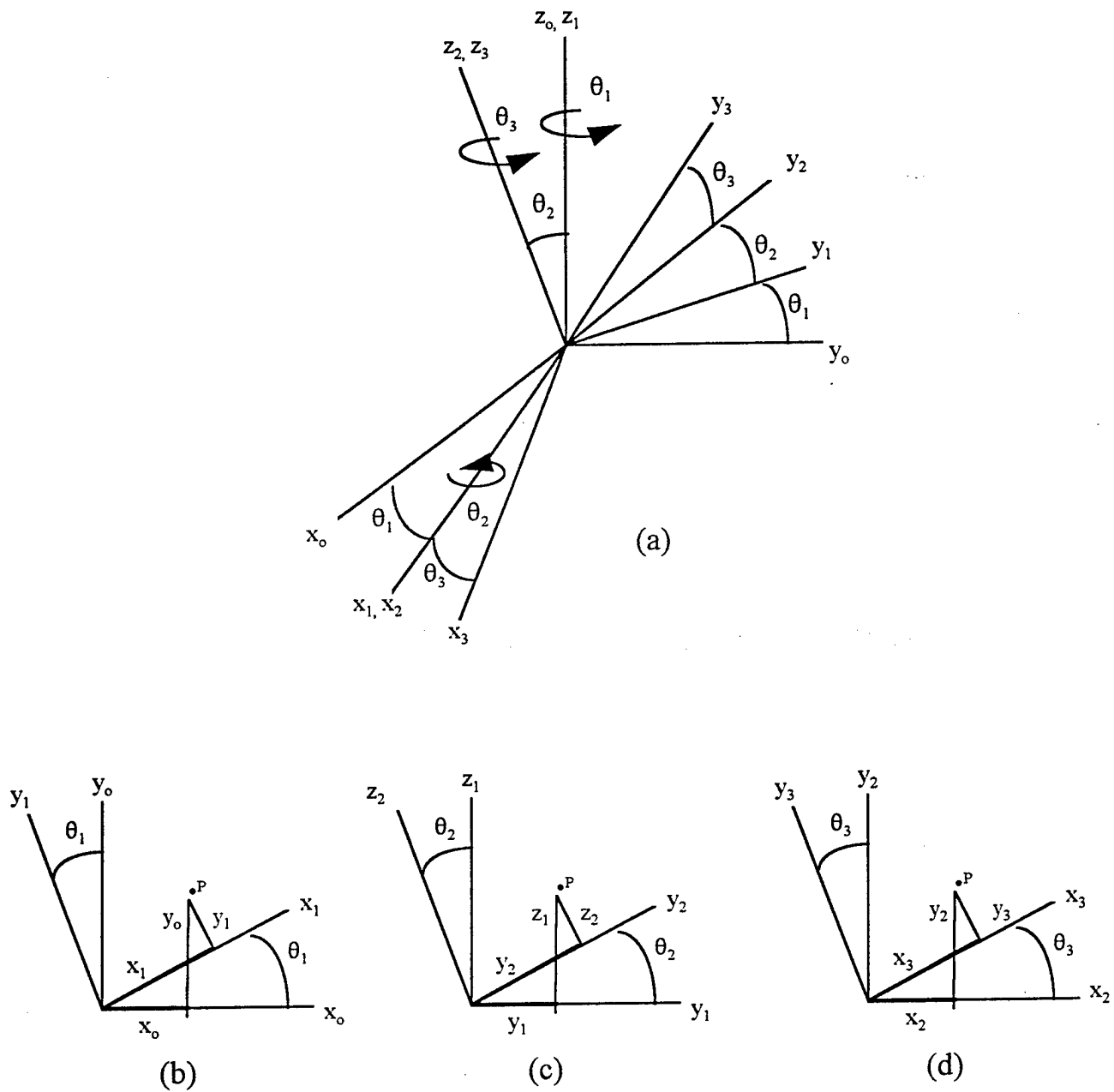


Fig. 8 Three consecutive rotations from the geometry coordinate system to the material coordinate system

the tensor. Conventionally, the velocity gradient is simply partitioned into the strain-rate (symmetric) tensor  $[D]$  and spin (anti-symmetric) tensor  $[W]$ ,

$$[L] = [D] + [W] \quad (36)$$

It is noted from the definition of  $[L]$  that  $[D]$  and  $[W]$  depend on the instantaneous rate of deformation of the current configuration. On the other hand,  $[L]$  can also be expressed in terms of  $[U]$  and  $[R]$  which relate the current configuration to the reference GGCS by using the right decomposition from (34) in (35),

$$[L] = [R]_{ox}[L]_o[R]_{ox}^T + [\Omega] \quad (37)$$

where

$$[L]_o = [\dot{U}][U]^{-1} \quad \text{and} \quad [\Omega] = [\dot{R}]_{ox}[R]_{ox}^T \quad (38)$$

Substitution of the identity matrix,  $[I]$ , for  $[R]$  into Eqs. (37) and (38) indicates that  $[L]_o$  is a velocity gradient referred to the unrotated (not reference) configuration. Thus, similar to Eq. (36),  $[L]_o$  may be partitioned into the strain rate tensor  $[D]_o$  and spin tensor  $[W]_o$  in the unrotated frame

$$[L]_o = [D]_o + [W]_o \quad (39)$$

Also, the following relationships can be derived

$$[D]_o = [R]_{ox}^T[D][R]_{ox} \quad \text{and} \quad [\Omega] = [W] - [R]_{ox}[W]_o[R]_{ox}^T \quad (40)$$

It can be seen from Eq. (37) by letting  $[U]=[I]$  in Eq. (38) that  $[\Omega]$  represents the rate of rigid-body rotation at a material point. It is equally simple to show that  $[W]$  represents the rate of rotation of the principal axes of the strain rate  $[D]$ . Both rotation tensors are anti-symmetric. However,  $[\Omega] = [W]$  if and only if  $[L]_o$  is symmetric, which in general fails to be so although  $[U]$  is always symmetric.

With  $[D]$  and  $[W]$ , the objective Jaumann stress rate  $[\dot{\sigma}]_j$  is written as,

$$[\dot{\sigma}]_j = [\dot{\sigma}]_x - [W][\sigma]_x + [\sigma]_x[W] \quad (41)$$

and

$$[\dot{\sigma}]_j = \Psi_x([\sigma]_x, [D]) \quad (42)$$

where  $[\sigma]_x$  is the Cauchy stress in the current configuration and  $\Psi_x$ , in general, is an anisotropic function of a symmetric 2nd-order tensor.

As proved by Johnson and Bammann [32], the Cauchy stress rate referred to the unrotated configuration is also material frame objective. The relationships among the unrotated and rotated Cauchy stress rates,  $[\dot{\sigma}]_o$  and  $[\dot{\sigma}]_x$ , and the Green-Naghdi stress rate  $[\dot{\sigma}]_p$  are given as

$$[\dot{\sigma}]_p = [\dot{\sigma}]_x - [\Omega][\sigma]_x + [\sigma]_x[\Omega] = [R]_{ox}[\dot{\sigma}]_o[R]_{ox}^T \quad (43)$$

The two Cauchy stresses are related by

$$[\sigma]_o = [R]_{ox}^T[\sigma]_x[R]_{ox} \quad (44)$$

Note that the Green-Naghdi stress rate and the Jaumann rate are very similar in form. Although they are all objective, the advantage of the unrotated Cauchy stress rate and the Green-Naghdi rate over the Jaumann rate is that the first two are truly a measure of the rate of change of stress, while the last has no conjugate measure of finite strain associated with it. In addition, the Jaumann rate will lead to a

nonsymmetric stiffness tensor between the rates of stress and deformation unless the material is incompressible [32].

The rate type constitutive equations for the unrotated Cauchy stress rate and Green-Naghdi rate can be generally expressed as

$$[\dot{\sigma}]_o = \Psi_o([\sigma]_x, [D]_o) \quad \text{and} \quad [\dot{\sigma}]_p = \Psi_x([\sigma]_x, [D]) \quad (45)$$

The second constitutive law in Eq. (45) is identical to Eq. (42); however, the rotated Cauchy stress rate calculated from Eqs. (41) and (43) is, in general, different. Equation (45) can be used to evaluate stress rate, but it is convenient to evaluate the stresses and then examine the failure modes in the material frame for fiber composites. This can be achieved by rotating the strain-rate  $[D]$  and the previous Cauchy stress tensors back to the MCS. The transformation matrix  $[R]$  from the current frame to the MCS is simply the product of the two matrices

$$[R] = [R]_{ox} [R]_{om} \quad (46)$$

in which  $[R]_{om}$  is given in Eq. (33). Of consequence, the following transformations exist

$$[\sigma]_m = [R]^T [\sigma]_x [R] \quad \text{and} \quad [\sigma]_x = [R] [\sigma]_m [R]^T \quad (47)$$

$$[D]_m = [R]^T [D] [R] \quad \text{and} \quad [D] = [R] [D]_m [R]^T \quad (48)$$

The subscript  $m$  in the above equations represents the quantities in the material frame. With  $[D]_m$  obtained from Eq. (48), the increments of volumetric and deviatoric strains in the material coordinates can be decomposed. Therefore, one can calculate the stress rate  $[\dot{\sigma}]_m$  using the EOS and the anisotropic elasto-plasticity theory developed in Section 2.1, and then update the current stress  $[\sigma]_m$ . As pointed out by Flanagan and Taylor [31], one of the most challenging tasks in large deformation analysis is to determine the rotation tensor  $[R]_{ox}$ . Multiplying the second equation in Eq. (38) by  $[R]_{ox}$  yields,

$$[\dot{R}]_{ox} = [\Omega] [R]_{ox} \quad (49)$$

Direct integration of Eq. (49) gives the total rotation tensor  $[R]_{ox}$ . However, the orthogonality of  $[R]_{ox}$  degenerates rapidly no matter how fine a time increment used in the integration [31].

In the SPH numerical analysis, field variables are evolved incrementally. The geometry configuration is updated every time step, while the reference GGCS remains the same. Thus, the above transformation algorithm can be considered as for a single time step. To trace the principal material axes, the current, total rotation  $[R]_{ox}$  at each SPH particle should be estimated during the entire solution course.

An alternative approximation algorithm for the rate integration of  $[R]_{ox}$ , which was proposed by Hughes and Winget [33], was employed. The total rotation  $[R]_{ox}$  at time  $t + \Delta t$  is updated via

$$[R]_{t+\Delta t, ox} = [\mathcal{Q}_{\Delta t}] [R]_{t, ox} \quad (50)$$

where  $\{x_{t+\Delta t}\} = [\mathcal{Q}_{\Delta t}] \{x_t\}$ . With the assumption of a constant rate of rotation over a time increment, the approximation of Eq. (50) is given as

$$([I] - \frac{1}{2} \Delta t [\Omega]) [R]_{t+\Delta t, ox} = ([I] + \frac{1}{2} \Delta t [\Omega]) [R]_{t, ox} \quad (51)$$

The initial conditions for  $[R]_{ox}$  is the unit identity matrix.

Before the calculation of Eq. (51),  $[\Omega]$  must be determined. Substituting Eq. (34) into (35), postmultiplying by  $[V]$ , and regrouping results in

$$[\dot{V}] = [L][V] - [V][\Omega] \quad (52)$$

Since the tensors  $[\Omega]$  and  $[W]$  have only three independent components, for convenience, two dual vectors based on the right-handed rates of rotation can be defined

$$\Omega_{ij} = e_{ikj} \omega_k \quad (53)$$

$$W_{ij} = e_{ikj} w_k \quad (54)$$

Substituting Eqs. (36), (53) and (54) into (52) results in

$$\{\omega\} = \{w\} + ([I] \text{tr}([V]) - [V])^{-1} \{z\} \quad (55)$$

in which

$$z_i = e_{ikj} D_{jm} V_{mk} \quad (56)$$

Making use of Eqs. (53), (55) and (56), the rotation rate tensor  $[\Omega]$  can be evaluated once the velocity gradient  $[L]$  and the left stretch tensor  $[V]$  are determined. Note that the matrix  $[L]$  is computed using the velocity components obtained from the momentum equations. The matrix  $[V]$  is time integrated using Eq. (52) with an initial condition corresponding to the initial state of stress. For an undeformed state, normally the stretch is set to the identity tensor  $[I]$ .

### 3.5 SMOOTHED PARTICLE HYDRODYNAMICS

SPH is a pure Lagrangian particle method, which was introduced by Lucy [34] and Gingold and Monaghan [35] in 1977. It has been successfully applied to astrophysics and shock physics since then as well as to hypervelocity impact of solid materials in the early 1990's [17]. The power of SPH is that no underlying grids are required. It not only avoids the numerical difficulties of mesh entanglement and distortion during the loading process as often occur in the finite element and finite difference analyses but also lends itself to the treatment of initiation and growth of cracks. Thus, in addition to the ballistic limits and residual velocities, the detailed damage progression, such as perforation, matrix cracking, fiber breakage, delamination, fragmentation, etc., can naturally be simulated with this unique technique.

The foundation of SPH is the interpolation theory. Through the use of kernel estimates, the partial differential equations of the three conservative laws of continuum mechanics can be transformed into integral forms. Numerically, these integral equations are approximated in terms of the field variables at a set of disordered points (particles). These field variables are then directly evolved from the interactions among particles using an explicit time integration scheme. Therefore, no matrix equation solving is required. The details of the SPH formulation for solid materials can be found in Libersky et al. [17].

In the present study, the capability of the SPH for isotropic materials is extended to include fiber-reinforced composites. The anisotropic, elasto-plastic constitutive law, equation of state, rate-dependent failure criterion for the AS4/3501-6 composites, as well as the stress and strain transformations between material and geometric coordinate systems under large rotation described in the previous sections were incorporated into the hydro code MAGI.

## 4. NUMERICAL RESULTS AND DISCUSSION

The main purpose of this program is study the feasibility of the SPH for 3-D composite laminate penetration. Before doing that, the credibility of the modified MAGI code, named CMAGI, was first verified. The resolution dependency of the number of particles on the SPH solution was also investigated. An aluminum plate impacted by a steel rod was considered for the former, and the AS4/3501-6 composite laminates impacted by a steel rod were studied for the latter. These calculations were performed under the plane strain assumption. In the 3-D simulations, normal impact of a steel cube striking at the center of the 8-layer AS4/3501-6 composite laminates were conducted. Three impact velocities (V) were investigated: 0.2 km/s, 0.6 km/s and 2.0 km/s. For the sake of clarity, the results of damage in the targets presented in the following are confined to specific critical regions.

### 4.1 VALIDATION OF THE MODIFIED MAGI CODE

The credibility of the CMAGI code for the composite materials was verified with the case of normal impact of a square steel rod striking at the center of an aluminum plate. Plane strain condition was assumed. The width and thickness of the cross-section of the target are 1.93 cm and 0.0965 cm, respectively. The size of the square projectile is 0.386 cm. The impact speed was set at 2.0 km/s. Due to symmetry, only half of the domain was analyzed. Two calculations were carried out using the MAGI code (isotropic material version) and the CMAGI code, respectively. The aluminum target was modeled as a single material for the former while it was treated as an 8-layer "composite" for the latter. For the comparison purpose, no failure was assumed for the aluminum target since the failure model proposed in the CMAGI is different from that used in the MAGI.

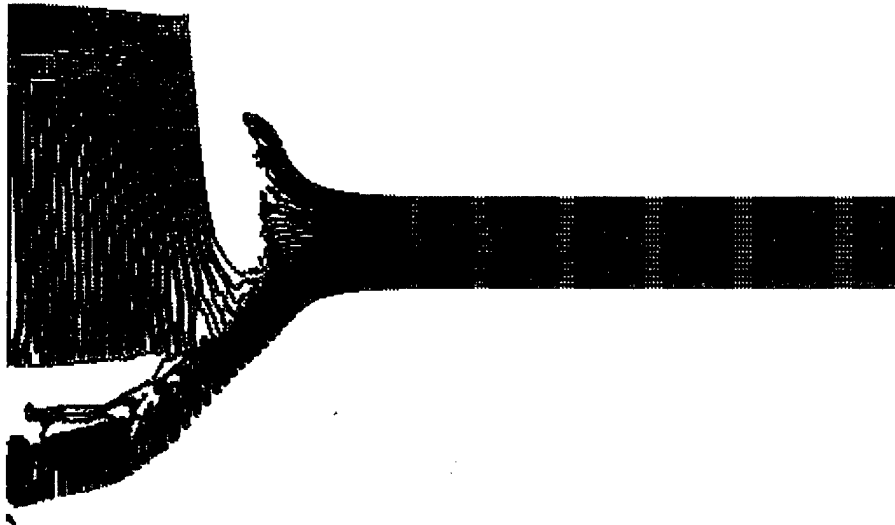
Figure 9 shows the deformation configurations for the aluminum target and steel projectile at 1.0  $\mu$ s predicted using the CMAGI and MAGI codes. It is seen from the figure that the overall responses are similar but the local deformations are different.

The discrepancy of the local deformations could be caused by the stress scaling back algorithm. The MAGI code brings the stress deviators  $s_{\alpha\beta}$  back to the yield surface from the overshooting, elastic stress state based on the assumption,

$$s_{\alpha\beta} = s_{\alpha\beta}^e \sqrt{Y_o / 3J_2^2} \quad (57)$$

where  $s_{\alpha\beta}^e$  are the overshooting deviatoric stresses evaluated using the linear elasticity;  $J_2$  and  $Y_o$  are the von Mises stress and the material yield stress, respectively. It should be noted that Eq. (57) is suitable only for the cases that all deviatoric stresses are increasing in ratio. In the impact events, the loading could be history-sensitive; therefore, the accuracy of using Eq. (57) is questionable. In the CMAGI, the elastic-plastic stress calculation is carried out using the scaling factor approach as previously mentioned. Obviously the present approach would predict more accurate results.

The other possible reason for the different local deformations could be the stress and strain transformations between the undeformed and deformed configurations. No transformation is included in the MAGI code.



(a) isotropic material approach



(b) composite laminate approach

Fig. 9 Aluminum target and steel projectile deformation at  $1.0 \mu\text{s}$



## 4.2 SPH SOLUTION ACCURACY AS A FUNCTION OF NUMBER OF PARTICLES

Two different AS4/3501-6 composite laminates,  $[0_8]$  and  $[0/90/45/-45]_s$ , were considered for studying the resolution dependency of the SPH solution as a function of number of particles. Normal impact at the center of the plates and plane strain condition were assumed. The width and thickness of the cross-section of both composite targets are 4.0 cm and 0.0965 cm, respectively. The size of the square steel projectile is 0.386 cm. The striking speed of the projectile was set at 2.0 km/s. On account of the symmetry, only half of the domain was analyzed. For each impact case, two different SPH models were set up. One model consisted of six particles per layer, and the other model had two particles per layer. Of course, the simulation with more particles required more computer memory and time than that with less particles.

Figure 10 presents the impact results at 3.0  $\mu$ s for the  $[0_8]$  laminate modeled with six particles per layer. The pink-colored particles in Fig. 10b are damaged. Delamination is clearly present between the 2nd and 3rd layers (from the bottom). The damaged zone is about three times the projectile size. The results predicted with two particles per layer are shown in Fig. 11. Although delamination is not clearly shown as in Fig. 10, the patterns and sizes of the damage predicted by the two models are close.

The impact results at 3.0  $\mu$ s for the  $[0/90/45/-45]_s$  laminate predicted with 6 particles and 2 particles per layer are shown in Figs. 12 and 13, respectively. The sizes of the perforation holes are close for the two predictions; however, the six particles model results in more damage than the two particles model.

The above results imply that in order to accurately predict damage, a composite structure with different fiber orientations or material systems requires finer particles than a single material structure.

## 4.3 3-D SIMULATIONS OF COMPOSITE LAMINATE PENETRATION

All the WL AS4/3501-6 composite specimens measured 20.32x20.32 cm and were clamped around the periphery. The unsupported surface was 17.78x17.78 cm. Each laminar is 0.01206 cm thick. Two different fragment projectiles were of interest. One was prismatic with the dimensions of 0.584x0.584x0.724 cm, and the other was cubic with a side length of 0.970 cm.

As shown in Section 4.2, a SPH model with two particles per layer is not able to predict accurate damage results for the  $[0/90/45/-45]_s$  laminate. For the WL 8-ply laminates, the ratio between the length of the free surface and thickness is about 184. Thus, the number of particles required to modeled a quadrant of the plates will be over 8.6 millions even though only two particles are modeled in one layer. This makes it formiably difficult to simulate the WL penetration tests. Therefore, it was our intent to conduct the 3-D composite laminate penetration calculations for demonstrating the SPH capability rather than for simulating the real WL tests.

In the following 3-D calculations, normal impact simulations of a steel fragment striking at the center of the AS4/3506-1 composite plates were carried out. The laminate considered here is an 8-layer composite with the in-plane dimensions of 4.0x4.0 cm. The cubic projectile is a steel fragment. Each size is 0.386 cm long (four times the laminate thickness). No constraints are imposed on the composite target. For convenience, only the first quadrant of the plate was modeled with one particle per layer. The numbers of particles composing the projectile and the composite are 8,192 and 217,800, respectively. It should be noted that the quasi-isotropic laminate considered here exhibits the bending twist coupling.



(a) deformation

(b) damage pattern

Fig. 10 8-layer unidirectional composite impacted by a steel rod at  $3.0 \mu\text{s}$ ,  $V=2.0 \text{ km/s}$   
(6 particles per layer)

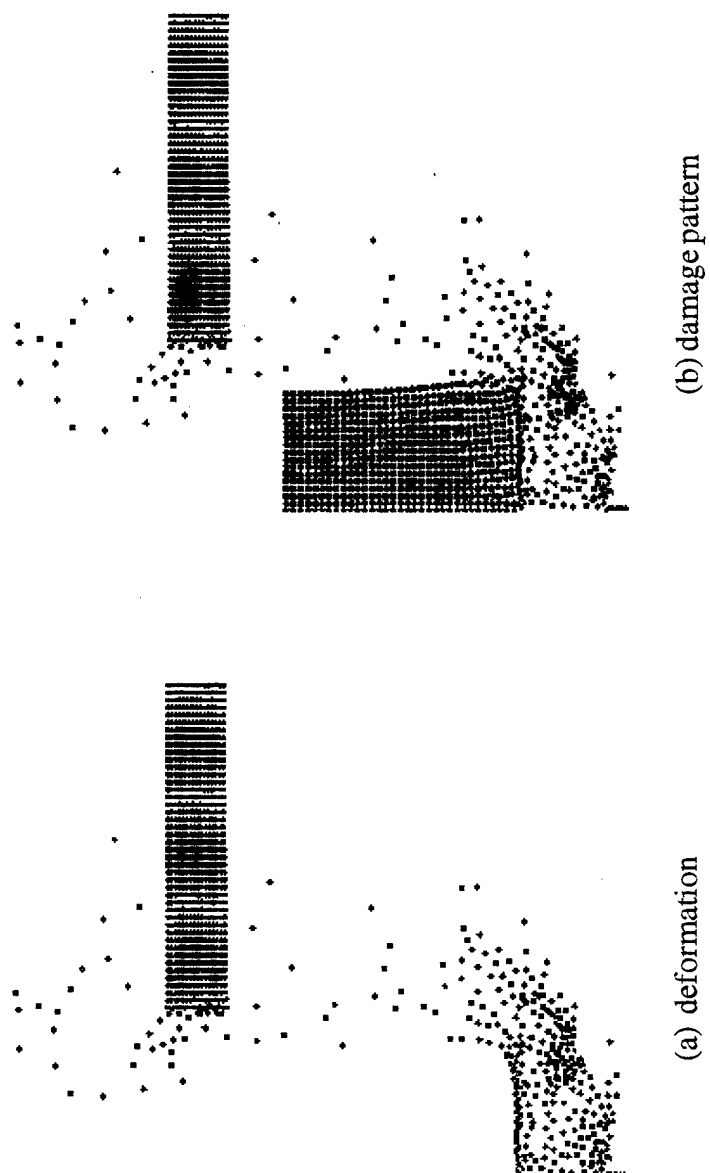


Fig. 11 8-layer unidirectional composite impacted by a steel rod at  $3.0 \mu\text{s}$ ,  $V=2.0 \text{ km/s}$   
(2 particles per layer)

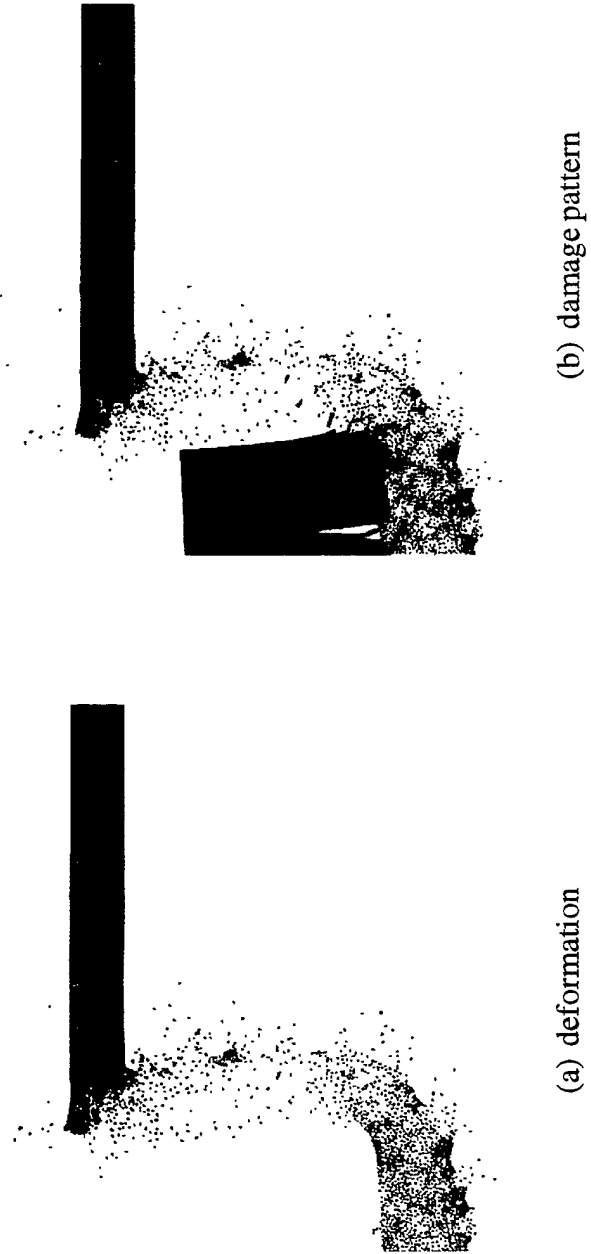


Fig. 12 The  $[0/90/45/-45]_s$  laminate impacted by a steel rod with  $V=2.0$  km/s at  $3.0 \mu s$   
(6 particles per layer)

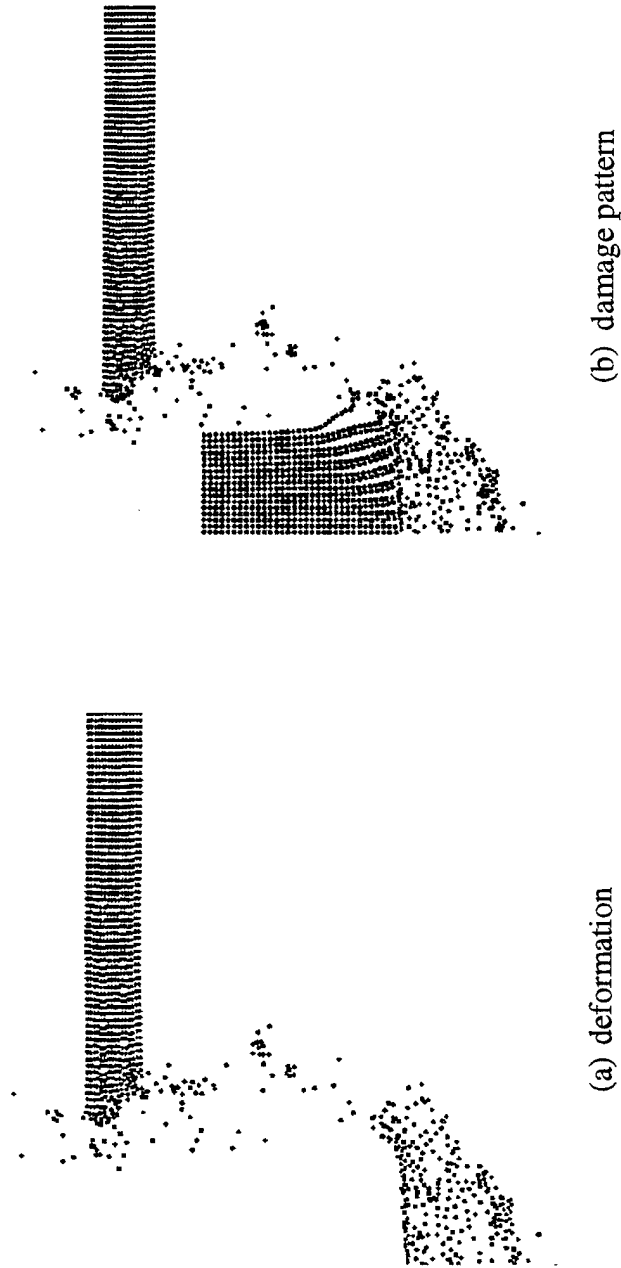


Fig. 13 The  $[0/90/45/-45]_s$  laminate impacted by a steel rod with  $V=2.0$  km/s at  $3.0 \mu\text{s}$   
(2 particles per layer)

Strictly speaking, an entire plate or a half of the plate with a special treatment of the cut boundary should be analyzed.

#### **Case 1: [0/90/45/-45]<sub>s</sub> laminate impacted at 2.0 km/s**

Figure 14 presents the predicted deformation states at different penetration stages for the [0/90/45/-45]<sub>s</sub> laminate impacted at 2.0 km/s. The length of each size of the plate shown in the figure is 0.6 cm. As seen in Figs. 14c and d, the perforation process completed between 1.0  $\mu$ s and 2.0  $\mu$ s. Ejectas are found in Fig. 14d. They are originated from the top layer where the fibers are perpendicular to the size of the projectile. Figure 15 shown the different views of the deformation configurations at 3.0  $\mu$ s. The damage at this time is considered as the final damage state although there was a small amount of additional deformation still to occur. It is visually indicated that the composite laminate remains in good shape except for the vicinity of the impact region. The damage pattern at the cross-sections of  $x=0$ ,  $y=0$ , and  $x=y$  are plotted in Fig. 16. The length of the cross-section shown in this figure is 1.0 cm. The particles with yellow color are damaged with at least one failure mode. As shown in Fig. 16, the perforation hole is about 30% larger than the size of the projectile. Although the present model of one particle per layer can not exactly predict delamination, the damage pattern at  $y=0$  (i.e.  $x$ -axis) is similar to that reported by Czarnecki [36]. In Ref. 36, the quasi-isotropic 32-ply laminate was made of the same [0/90/45/-45] family. The damage sustained near the laminate rear face was extreme delamination several times the diameter of the spherical projectile.

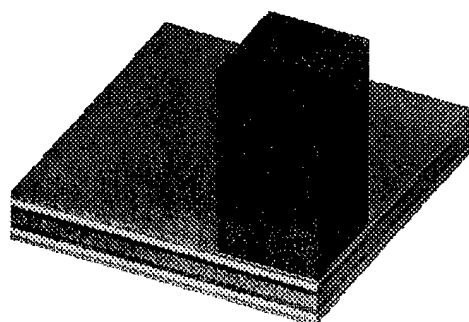
#### **Case 2: [45/-45/0/90]<sub>s</sub> laminate impacted at 2.0 km/s**

The deformation at 3.0  $\mu$ s for the [45/-45/0/90]<sub>s</sub> laminate impacted at 2.0 km/s is shown in Fig. 17. The length of each size of the plate shown in the figure is 0.6 cm. No ejecta is found in this case. The size of the perforation is close to that in the [0/90/45/-45]<sub>s</sub> laminate impacted by the same speed. Figure 18 indicates the damage patterns at the cross-sections of  $x=0$ ,  $y=0$ , and  $x=y$ . The length of the cross-section shown in Fig. 18 is 1.0 cm. The detailed damage in the vicinity of the perforation is different from that seen in the [0/90/45/-45]<sub>s</sub> laminate. At  $x=0$ , the dominating damage in the second and seventh plies is much severer in the [45/-45/0/90]<sub>s</sub> laminate than that in the [0/90/45/-45]<sub>s</sub> laminate. At  $y=0$ , the damage occurs evenly in the two -45 degree plies and the 0-degree layer in this case instead of the triangular damage zone found in the three bottom layers for the [0/90/45/-45]<sub>s</sub> laminate (Fig. 16b). The difference is less pronounced for the cross-section of  $x=y$ .

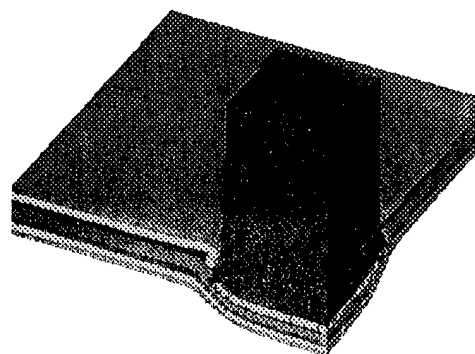
#### **Case 3: [45/-45/0/90]<sub>s</sub> laminate impacted at 0.6 km/s**

Figure 19 shows the deformation at 10.0  $\mu$ s for the [45/-45/0/90]<sub>s</sub> laminate impacted at 0.6 km/s. The length of each size of the plate shown in the figure is 1.0 cm. It is interesting to note the results in Fig. 19b. A strip of damage extends along the 45 degree direction from the corner of the perforation. This damage pattern is similar to the C-SCAN inspection (Fig. 20) made by the Wright Laboratory [37]. Figure 21 presents the detailed damage at the cross-sections of  $x=0$ ,  $y=0$ , and  $x=y$ . The length of the cross-section shown in the figure is 1.5 cm. The front size of the perforation is close to the size of the projectile, while the rear size is larger. In general, the perforation hole is smaller than that caused by the striking speed of 2.0 km/s. The damage along the 45-degree direction is clearly indicated in Fig. 21c. It occurs in the two bottom layers and the top layer and is several times the size of the projectile.

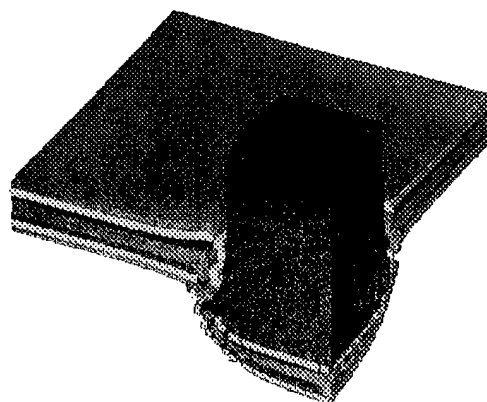
The penetraion simulation for the second quadrant of the plate was also carried out. No damage was



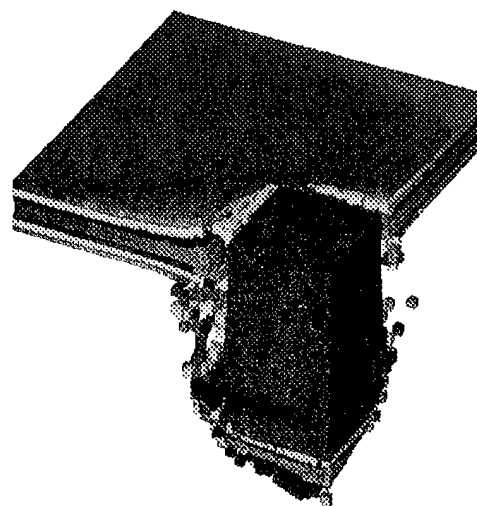
(a)  $t = 0$



(b)  $t = 0.5 \mu\text{s}$



(c)  $t = 1.0 \mu\text{s}$



(d)  $t = 2.0 \mu\text{s}$

Fig. 14 Penetration at different stages for the  $[0/90/45/-45]_s$  laminate impacted by a steel cube with  $V=2.0 \text{ km/s}$

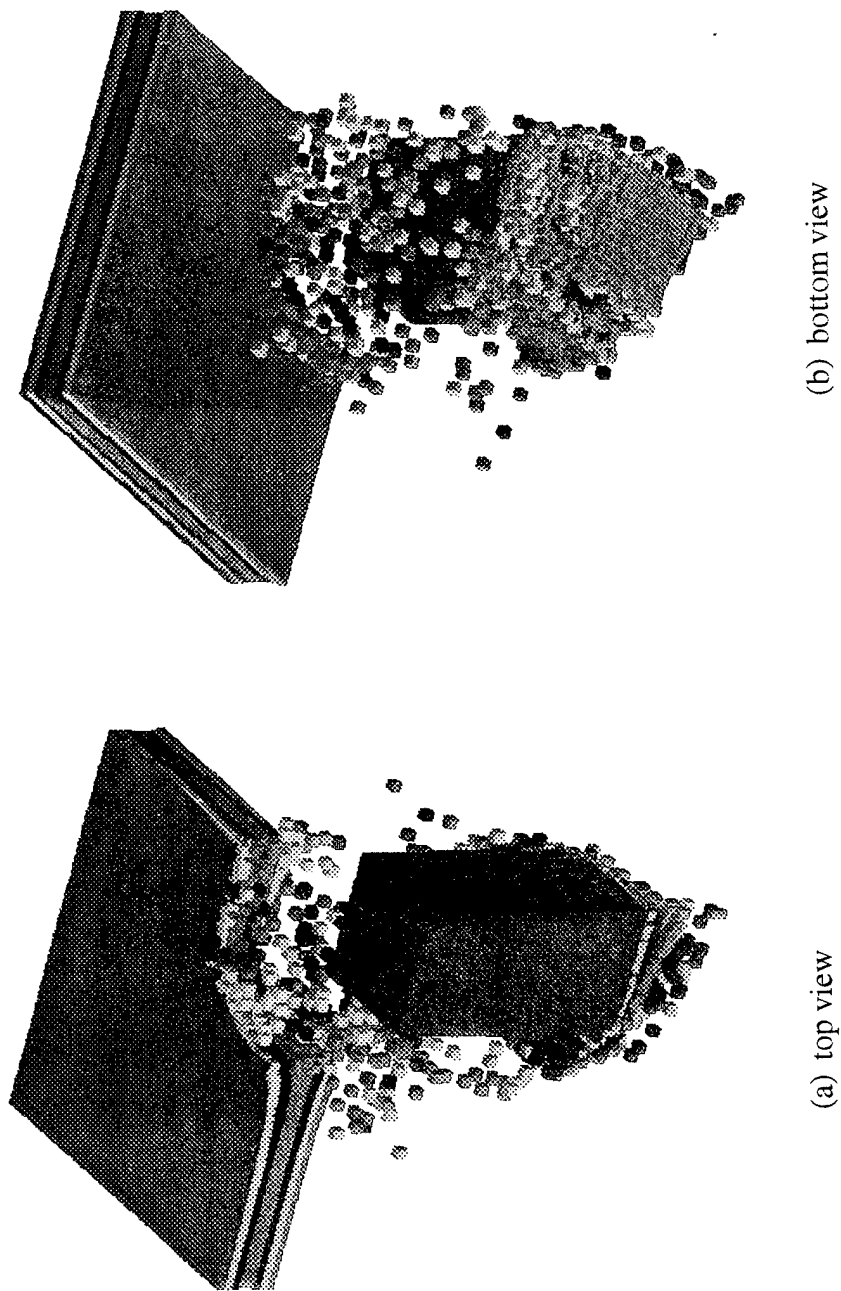
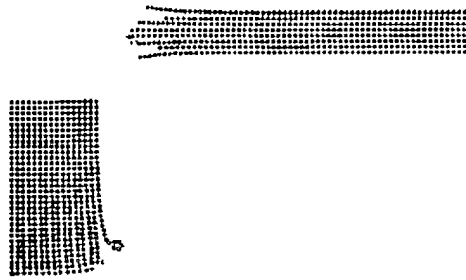
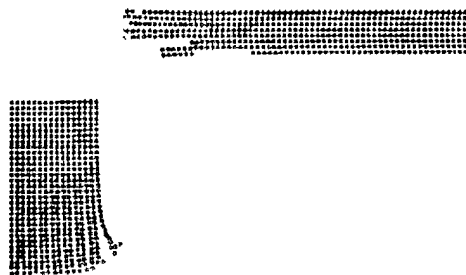


Fig. 15 Deformation at  $3.0 \mu\text{s}$  for the  $[0/90/45/-45]_s$  laminate impacted by a steel cube with  $V=2.0 \text{ km/s}$

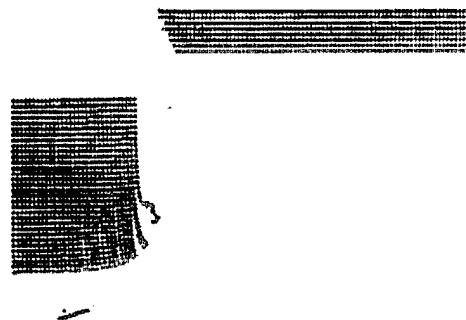




(a)  $x=0$

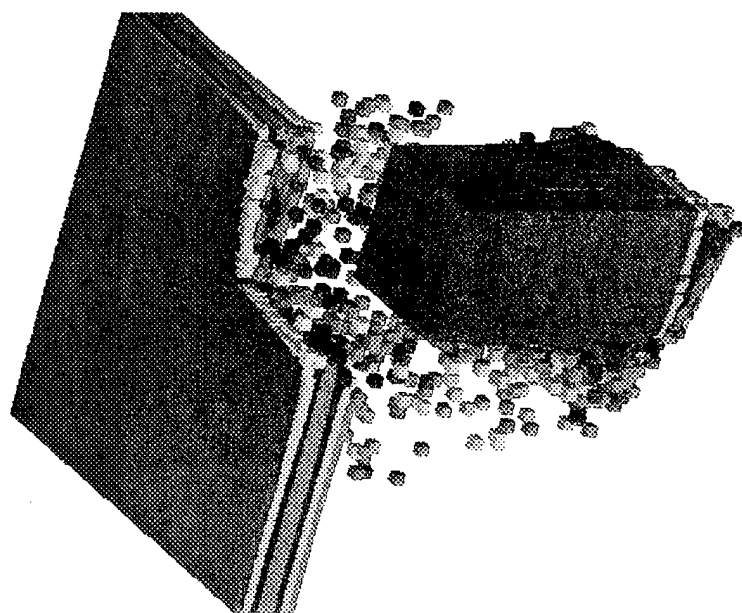


(b)  $y=0$

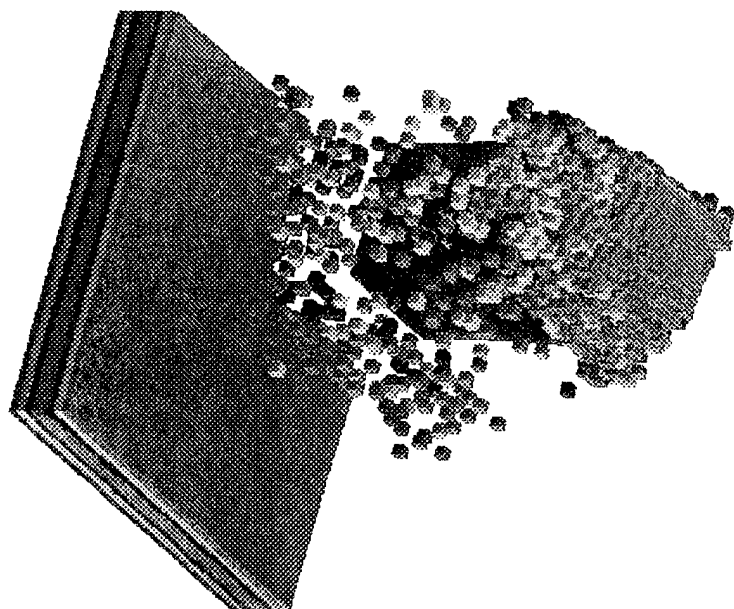


(c)  $x=y$

Fig. 16 Damage pattern at the cross-sections of  $x=0$ ,  $y=0$ , and  $x=y$  in the  $[0/90/45/-45]_s$  laminate impacted by a steel cube with  $V=2.0$  km/s at  $3.0 \mu s$

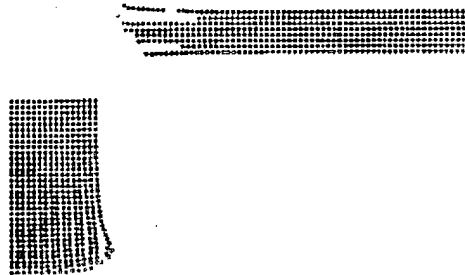


(a) top view

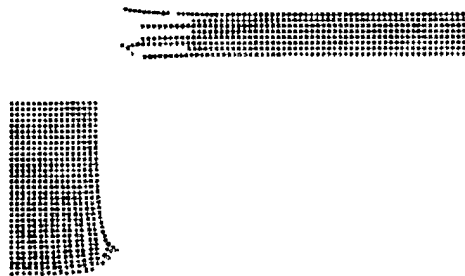


(b) bottom view

Fig. 17 Deformation at  $3.0 \mu\text{s}$  for the  $[45/-45/0/90]_s$  laminate impacted by a steel cube with  $V=2.0 \text{ km/s}$



(a)  $x=0$

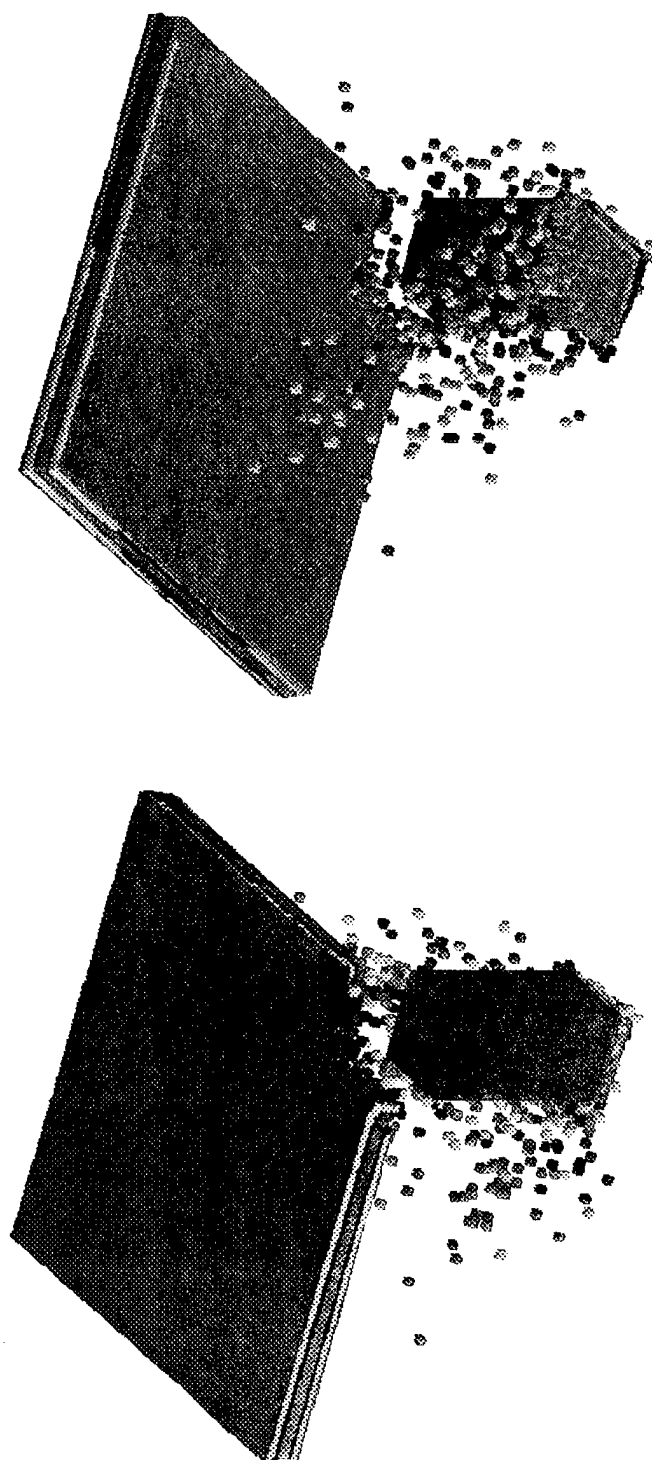


(b)  $y=0$



(c)  $x=y$

Fig. 18 Damage pattern at the cross-sections of  $x=0$ ,  $y=0$ , and  $x=y$  in the  $[45/-45/0/90]_s$  laminate impacted by a steel cube with  $V=2.0$  km/s at  $3.0 \mu s$



(b) bottom view

(a) top view

Fig. 19 Deformation at  $10.0 \mu\text{s}$  for the  $[45/-45/0/90]_s$  laminate impacted by a steel cube with  $V=0.6 \text{ km/s}$

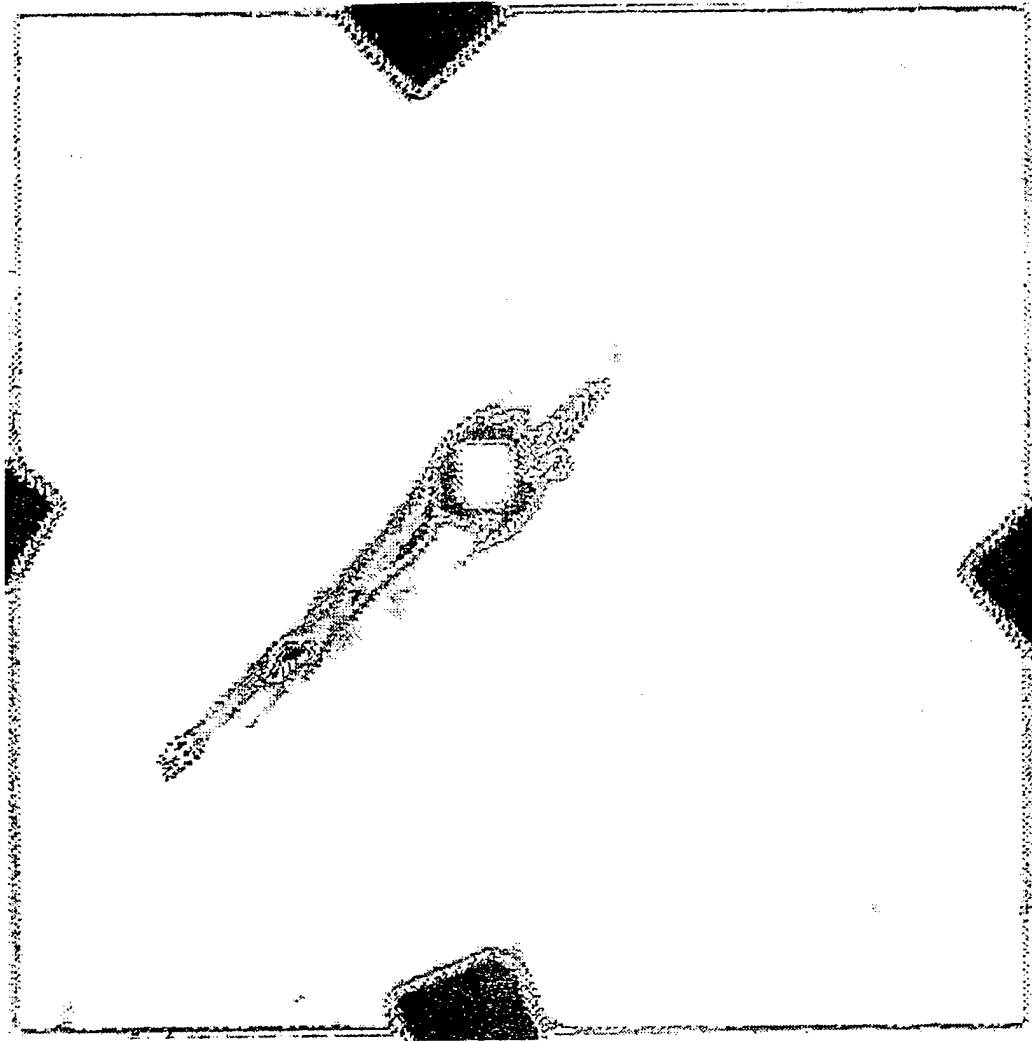
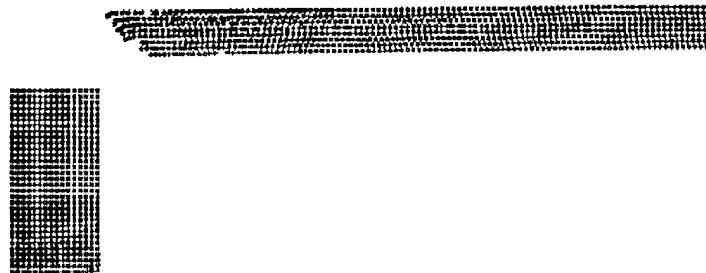
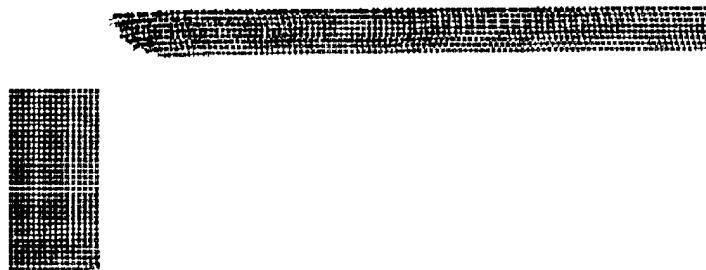


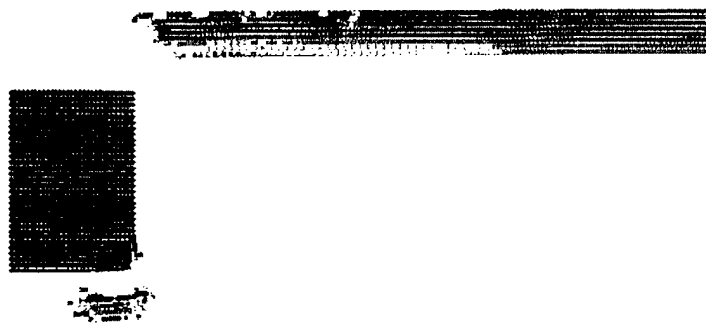
Fig. 20 A representative damage pattern in the  $[45/-45/0/90]_s$  laminate impacted by a steel cube measured using C-SCAN [24]



(a)  $x=0$



(b)  $y=0$



(c)  $x=y$

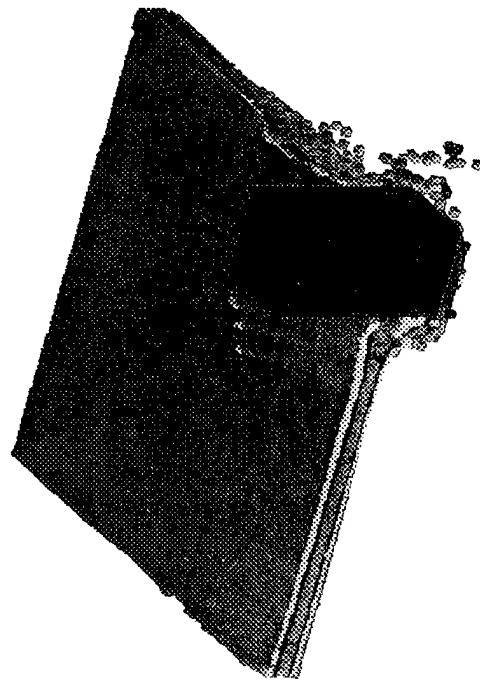
Fig. 21 Damage pattern at the cross-sections of  $x=0$ ,  $y=0$ , and  $x=y$  in the  $[45/-45/0/90]_s$  laminate at  $10.0 \mu s$  after impact by a steel cube at  $V = 0.6 \text{ km/s}$

found on the top and bottom faces except in the vicinity of the perforation. This is consistent with the experimental result shown in Fig. 20.

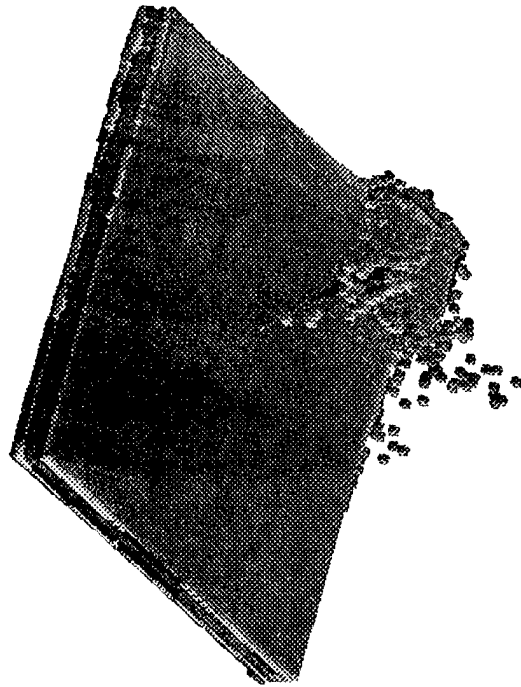
**Case 4: [45/-45/0/90]<sub>s</sub> laminate impacted at 0.2 km/s**

The deformation at 10.0  $\mu$ s for the [45/-45/0/90]<sub>s</sub> laminate impacted at 0.2 km/s is presented in Fig. 22. The length of each side of the plate shown in the figure is 1.0 cm. The penetration process is not completed yet at this time. Note again the strip of damage that extends along the 45 degree direction from the corner of the perforation (Fig. 22b). The width of the strip is greater than that found in the case of the 0.6 km/s impact speed. The final damage in the entire quadrant of the composite plate (at 30.0  $\mu$ s) is shown in Fig. 23. The perforation hole is larger in the x-direction than in the y-direction. The damage is found at many locations in both Figs. 23a and b. It is not clear if the prediction is reasonable or not for this case.

Figure 24 shows the deformed projectiles after impact at the striking speeds of 0.2, 0.6 and 2.0 km/s. It is clearly indicated in the figure that the projectile loses its mass at 2.0 km/s. The higher the impact speed, the severer the deformation of the projectile. The predicted residual velocities of the projectiles are about 0.185 km/s, 0.558 km/s and 1.885 km/s, respectively. The percentages of the residual velocities to the initial striking speeds are 92.5%, 93.0% and 94.2%, which are close to the measurement by the Wright Laboratory [37].



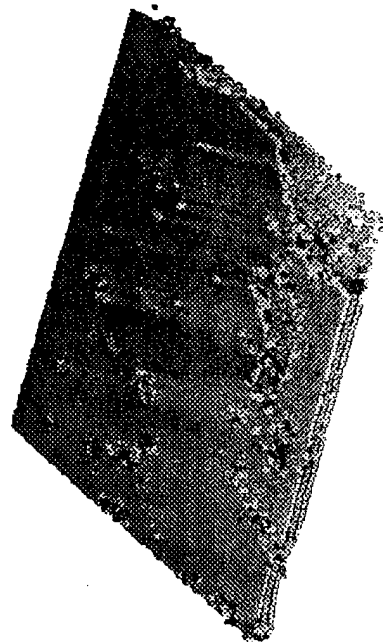
(a) top view



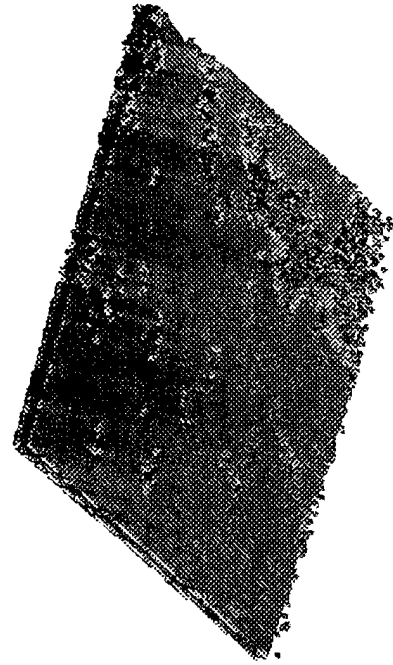
(b) bottom view

Fig. 22 Deformation at  $10.0 \mu\text{s}$  for the  $[45/-45/0/90]_s$  laminate impacted by a steel cube at  $V=0.2 \text{ km/s}$





(a) top view



(b) bottom view

Fig. 23 Damage in the  $[45/-45/0/90]_s$  laminate at  $30.0 \mu s$  after impact by a steel cube at  $V=0.2 \text{ km/s}$



$V = 0.2 \text{ km/s}$



$V = 0.6 \text{ km/s}$



$V = 2.0 \text{ km/s}$

Fig. 24 Deformation of the projectiles after impact at different striking speeds

## 5. CONCLUSIONS AND RECOMMENDATION

A physics-based "first principle" model for composite laminate penetration was developed and incorporated into the smoothed particle hydrodynamics code. The model includes various modules appropriate for fiber composites. They are an anisotropic elasto-plasticity constitutive model, an equation of state, a failure criterion, as well as stress and strain transformations between the material and geometric coordinate systems under large deformation. Due to the limitation of the computer memory and time, numerical simulations of 3-D composite laminate penetration were performed with an intent for the SPH capability demonstration rather than the real WL test simulation. Our results clearly demonstrate success in both accounts: (a) numerical simulation of composite laminate damage zone correlated well with the known experimental data, and (b) newly improved SPH proved to be a robust and viable analytical tool for predicting response of non-homogeneous, anisotropic composite materials to intensive dynamic loadings.

In conclusion, we have achieved the established goal of this task where a fundamental and economical analytical tool capable of predicting damage response of fiber-reinforced composites to impact loadings is developed. We submit however, there is a great deal more development needed before we can assess damage across a broad spectrum of composite structures. Following is a list of most pertinent topics:

- (1) generalization of the current developed anisotropic plasticity model and failure criterion for fiber-reinforced composites to encompass high strain-rate regime,
- (2) extension of the proposed equation of state for composites to include temperature and phase changes,
- (3) development of a tri-axial ellipsoidal smoothing function for prismatic particles, and
- (4) extension of the current SPH capability for interface and boundary condition applications.

The first two topics are straight forward. They heavily rely on experiment. The last two needs are explained as follows.

To overcome the computer memory problem and to improve the computational efforts, parallel computation could be one of the possible approaches. However, this method could be less attractive because the number of particles required for an accurate solution could be enormous. An alternative approach is the mixed finite element and SPH method. The critical regions, such as the vicinity of the projectile-target interaction and the possible damage zones, are modeled using the SPH, while the remote, non-critical area is analyzed using the finite element method. Again, this approach could be less intriguing. The reason is that damage zone in composite laminates could be large and, in turn, requires a huge number of particles to model. The other reason is that the boundary of the damage zone is unknown prior to the solution. Of consequence, the partition of the entire domain for the finite element method and SPH depends on one's luck. A more feasible approach, we believe, is to develop a tri-axial ellipsoidal smoothing function for prismatic particles [38-39]. A particle with a large aspect ratio of the in-plane dimension to thickness can tremendously reduce the total number of particles needed to model the composite laminate and the projectile. A technical problem of this approach is that an ellipsoidal kernel does not conserve angular momentum. Once the problem is solved, the benefits from this approach on computer memory and time as well as labor efforts are evident.

Because the damage in a composite laminate could significantly be influenced by the stress waves reflected from different types of boundary, the boundary conditions should properly be treated in high

velocity impacts. In the current CMAGI code, two boundary conditions are allowed: free and symmetric. The latter is imposed by introducing ghost particles. To treat the clamped boundary conditions as required by the WL tests, some additional technical work must and can be done.

## 6. REFERENCES

1. Walters, W. and B. Scott. 1990. "High Velocity Penetration of a Kevlar ® Reinforced Laminate," *Proceedings of 22nd International SAMPE Conference*, **22**:1078-1087.
2. Brar, N. S. *Penetration Mechanics of Composites*. UDR-TR-92-45, University of Dayton Research Institute, Dayton, Oh, 1992.
3. Bless, S. J. and D. R. Hartman. 1989. "Ballistic Penetration of S-2 Glass Laminates," *Proceedings of 21st Int. SAMPE international Conference*, **21**:852-866.
4. Zhu, G., W. Goldsmith and C. K. H. Dharan. 1992. "Penetration of Laminated Kevlar by Projectiles-I. Experimental Investigations," *Int. J. Solid Structures*, **29**:399-420.
5. Lee, S-W. R. and C. T. Sun. 1993. "Dynamic Penetration of Graphite/Epoxy Laminates Impacted by a Blunt-Ended Projectile," *Composite Science and Technology*, **49**:369-380.
6. Sun, C. T. and S. V. Potti. "High Velocity Impact and Penetration of Composite Laminates," *Proceedings of ICCM-9, Ninth International Conference of Composite Materials*, Madrid, Spain, July 1993, pp. 157-165.
7. Schonberg, W. P. and E. J. Walker. 1991. "Use of Composite Materials in Multi-Wall Structures to Prevent Perforation by Hypervelocity Impact," *Composite Structures*, **19**:15-40.
8. Cantwell, W. J. and J. Morton. 1990. "Impact Penetration of Carbon Fibre Reinforced Plastic," *Composites Science and Technology*, **38**:119-141.
9. Zhu, G., W. Goldsmith and C. K. H. Dharan. 1992. "Penetration of Laminated Kevlar by Projectiles-II. Analytical Model," *Int. J. Solid Structures*, **29**:421-436.
10. Sun, C. T. and S. V. Potti. "Modeling Dynamic Penetration of Thick Section Composite Laminates," AIAA-95-1203-CP, *36th AIAA/ASME/ASCE/AHS/ASC SDM Conference and AIAA/ASME Adaptive Structures Forum*, New Orleans, LA, April 1995, pp. 383-393.
11. Vinson, J. R. and J. M. Walker. "Ballistic Impact into Composite Sandwich Structures," *Proceedings of the American Society for Composites*, 9th Technical Conference, Newark, Delaware, September 1994, pp.491-499.
12. Vinson, J. R. and J. A. Zukas. 1975. "On the Ballistic Impact of Textile Body Armor," *J. Appl. Mech.*, **42**:263-268.
13. Blanas, A. M. *Finite Element Modeling of Fragment Penetration of Thin Structural Composite Laminates*, NATICK/TR-92/019, U.S. Army Natick Research, Development and Engineering Center, Natick, MA, 1992.
14. Anderson, C. E., P. E. O'Donoghue and D. Skerhut. 1990. "A Mixture Theory Approach for the Shock Response of Composite Materials," *J. Composite Materials*, **24**:1160-1178.
15. Anderson, C. E., P. A. Cox, G. R. Johnson and P. J. Maudlin. 1994. "A Constitutive Formulation for Anisotropic Materials Suitable for Wave Propagation Computer Programs-II," *Computational Mechanics*, **15**:201-223.
16. Chen, J. K., D. F. Medina and F. A. Allahdadi. "Dynamic damage of composite plates to high intensity loadings," *Dynamic Response and Behavior of Composites*, AD-Vol. 46, ed. C. T. Sun et al. ASME, 1995, pp. 17-27.
17. Libersky, L. D., A. G. Petschek, C. T. Carney, J. R. Hipp and F. A. Allahdadi. 1993. "High Strain Lagrangian Hydrodynamics, a Three-Dimensional SPH Code for Dynamic Material Response," *J. Computational Physics*, **109**:67-75.
18. Griffin, O. H., M. P. Kamat and C. T. Herakovich. 1981. "Three-Dimensional Inelastic Finite Element Analysis of Laminated composites," *J. Composite Materials*, **5**:543-560.
19. Hansen, A. C., D. M. Blackketter and D. E. Walrath. 1991. "An Invariant Based Flow Rule for

- Anisotropic Plasticity Applied to Composite Materials," *J. Appl. Mech.*, **58**:881-888.
20. Xie, M. and D. F. Adams. 1995. "A Plasticity Model for Unidirectional Composite Materials and Its Application in Modeling Composites Testing," *Composite Science and Technology*, **54**(1):11-22.
  21. Chen, J. K. and C. T. Sun. 1987. "Nonlinear Analysis of Interlaminar Stress in Graphite/Epoxy Laminates with and without Delamination Cracks," *Composite Structures*, **8**:271-285.
  22. Chen J. L. and C. T. Sun. 1993. "A Plastic Potential Function Suitable for Anisotropic Fiber Composites," *J. Composite Materials*, **27**:1379-1390.
  23. Dvorak G. J. and Y. A. Bahei-El-Din. 1982. "Plasticity Analysis of Fibrous Composites," *J. Appl. Mech.*, **49**:327-335.
  24. Chen, J. K., F. A. Allahdadi and C. T. Sun. "A Quadratic Yield Function for Fiber-Reinforced Composites," submitted to *J. Composite Materials*.
  25. Sun, C. T. and R. S. Vaidya. 1993. "On Predicting Elastic Moduli and Plastic Flow in Composite Materials Using Micromechanics," *Proceedings of the ASC 8th Technical Conference on Composite Materials*, Cleveland, pp. 841-849.
  26. Adams, D. F. and D. A. Crane. 1984. "Combined Loading Micromechanical Analysis of a Unidirectional Composite," *Composites*, **15**:181-192.
  27. Owen, D. R. J. and E. Hinton. 1980. *Finite Elements in Plasticity*, Pineridge Press Limited, Swansea, U.K.
  28. Kerley, G. I., CTH Reference Manual: The Equation of State Package, SAND91-0344, Sandia National Laboratories, Albuquerque, New Mexico, 1991.
  29. Randles, P. W. and J. A. Nemes. 1992. "A Continuum Damage Model for Thick Composite Materials Subjected to High-Rate Dynamic Loading," *Mech. Mater.*, **13**:1-13.
  30. Nemes, J. A. and P. W. Randles. 1994. "Constitutive Modeling of High Strain-Rate Deformation and Spallation Fracture of Graphite/PEEK Composites," *Mech. Mater.*, **19**:1-14.
  31. Flanagan, D. P. and L. M. Taylor. 1987. "An Accurate Numerical Algorithm for Stress Integration with Finite Rotations," *Comp Meth. in Appl. Mech. and Engrg.*, **62**:305-320.
  32. Johnson, G. C. and D. J. Bammann. 1984. "A Discussion of Stress Rates in Finite Deformation Problems," *Int. J. Solids & Structures*, **20**(8): 725-737.
  33. Hughes, T. J. R. and J. Winget. 1980. "Finite Rotation Effects in Numerical Integration of Rate Constitutive Equations Arising in Large-Deformation Analysis," *Int. J. Num. Meths. Engrg.*, **15**:1862-1867.
  34. Lucy, L. B., 1977. "A Numerical Approach to the Testing of the Fission Hypothesis," *Astron. J.* **82**:1013-1020.
  35. Gingold, R. A. and J. J. Monaghan. 1977. "Smoothed Particle Hydrodynamics: Theory and Application to Nonspherical Stars," *Mon. Not. Roy. Astr. Soc.*, **181**:375-389.
  36. Czarnecki, G. J. "Dual Mode Fracture of Composite Laminates Penetration by Spherical Projectiles," ICAS-92-5.6.2, 18th Congress of the International Council of the Aeronautics Science, Beijing, China, September 20-25, 1992.
  37. P. Pettit, Wright Laboratory.
  38. Luehr, C. P. and F. A. Allahdadi. "Several SPH Topics," presented at A Colloquium on Advances in Smoothed Particle Hydrodynamics, January 21-22, 1993, Albuquerque, New Mexico.
  39. Fulbright, M. S., W. Benz and M. B. Davies. 1995. "A Method of Smoothed Particle Hydrodynamics Using Spheroidal Kernels," *The Astrophysics Journal*, **440**:254-262.

## DISTRIBUTION LIST

**AUL/LSE**

**Bldg 1405 - 600 Chennault Circle  
Maxwell AFB, AL 36112-6424**

**1 cy**

**DTIC/OCP**

**8725 John J. Kingman Rd, Suite 0944  
Ft Belvoir, VA 22060-6218**

**2 cys**

**AFSAA/SAI**

**1580 Air Force Pentagon  
Washington, DC 20330-1580**

**1 cy**

**PL/SUL**

**Kirtland AFB, NM 87117-5776**

**2 cys**

**PL/HO**

**Kirtland AFB, NM 87117-5776**

**1 cy**

**WL/FIVSM**

**1901 Tenth Street, Bldg. 63  
Wright Patterson AFB, OH 45433-7605  
Ms. Patricia A. Pettit**

**4 cys**

**Official Record Copy**

**PL/WSAE**

**Dr. Jinn-Kuen Chen**

**8 cys**